

Imperial College
London

Platform for Microrobot Navigation

Nafiseh Vahabi

A thesis submitted in partial fulfilment of the requirements for the degree of
MRes in Medical Robotics and Image Guided Intervention and for the
Diploma of
Imperial College

Imperial College London

Department of Surgery and Cancer

September, 2014

Dr. Henry Ip

Dr. Vincenzo Curto

Prof. Guang-Zhong Yang

Acknowledgements

I would like to thank

Contents

List of Figures	iii
List of Tables	iv
List of Acronyms	v
1 Introduction	1
1.1 Literature review	2
1.1.1 Bioinspired microrobots	2
1.1.1.1 Flagella style microrobots	4
1.1.1.2 Plant-based microrobots	9
1.1.2 Actuation methods	10
1.1.3 Fabrication methods	10
2 Methods	13
2.1 Microrobot design	13
2.2 Microrobot fabrication	13
2.2.1 Nanoscribe	14
2.2.2 Scanning Electron Microscope (Scanning Electron Microscope (SEM))	16
2.3 Simulation	17
2.3.1 Modeling helical propulsion	18
2.3.1.1 Resistive force theory for microrobot with two degree of	
freedom	19
2.3.1.2 Resistive force theory for six degree of freedom	22
2.3.1.3 Regularized Stokeslet method	28
2.3.1.4 Slender body theory	29
2.3.2 Microrobot actutation	33
3 Results	39
3.1 Design and propulsion methods	39
3.2 Design and fabrication	39
4 Discussion	40
5 Conclusion and future work	41
References	42

List of Figures

1.1	System Architecture.	3
1.2	The illustration of both flagellum and cilia shapes and microdevices mimicked the flagellum and cilia structures. [15].	4
1.3	The propulsion mechanism of the smooth flagellum and a mastigonemes flagellum. The propulsion direction of smooth flagellum (top design) is opposite of flagella's propagation wave (second from the top). Their artificial design (blue structures) is based on their locomotion mechanism [4].	4
1.4	Three design of helical microswimmers [14].	5
1.5	The effect of the gravity on the microrobot motion direction and gravity compensation [9].	6
1.6	(a) The misalignment of helical angle α with differnt helix angle (b) the oscillation behaviour of the microswimmer with the high and low frequencies [23].	7
1.7	The prototype of microhelical device. (a) Scanning electron microscopic image of the micro polymer composite with the 2 vol.% nanoparticle fill factor and (b) 4 vol.% of nanoparticle fill factor. (c) The CAD model shows all the parameters required for the microhelical design [13].	8
1.8	Demonstrating the drilling motion of the nanotubes under rotating magnetic field [27].	8
1.9	The shape of the Xylem in differnt plants . [9].	9
1.10	(A) The stages were required to make a plant-based microrobot. (B) A microscopic image of the a xylem helical structure [4].	10
1.11	DLW steps. step 1 is writting helical microrobots, in step 2 microrobots were developed in isopropyl alcohol and step 3 is coating them by a layer of Ni and Ti. [17].	11
2.1	Fabrication diagram. The nanoscribe technology is employed for the fabrication process and it followed by analysing structure under SEM. The final stage (yellow block in third column) has not been tried in this project. . .	14
2.2	nanoscribe workflow. The stages are involved in 3D micro-printing with nanoscribe device is shown in the diagram [12].	15
2.3	Scanning Electron Microscop. The components of the SEM is shown in the diagram [24].	16
2.4	Simulation algorithm. The main components of implementing the simulation is shown in the diagram.	17
2.5	The essential helix parameters to design a helical microrobot [20].	19
2.6	[3].	19
2.7	A motion of an arbitrary filament [3].	20

2.8	Three dimation configuration for the helical microrobot with a magnetic spherical head. The origin of the helix coordinate is denoted with \mathbf{O}_h and \mathbf{x}_h is the central axis of the helix [9].	22
2.9	Regularized Stokeslet Method (RSM) and Slender Body Theory (SBT). In RSM the surface of helix filament separated by cross-sectional segmentation and each surface represents by Stokeslets (left image). In the SBT, the Stokeslets are arranged along the central filament line (righth image) [20]. .	30
2.10	(a) The principle coordinate frame based on the gravity and principle components of the matrices in equations 2.92 and 2.91. (b) Construction details of direction of the microswimmer ($\tilde{\mathbf{X}}$) [9].	35

List of Tables

1.1	Different types of microrobots and their fabrication method.	12
2.1	Microrobot's design comparisons	13

List of Acronyms

SBT Slender Body Theory

FBMS Fixed-beam Moving-sample

gwl General Writting Language

MPC Magnetic Polymer Composite

MBFS Moving-beam Fixed-sample

RFT Resistive Force Theory

RSM Regularized Stokeslet Method

SEM Scanning Electron Microscope

stl STereoLithography

Abstract

Structures and functions of microorganisms were made them suitable reference to design microrobots. Flagellar propulsion of microorganism such as E.coli is used as an efficient approach for modelling micro swimmers locomotion method in low Reynolds number regime. Microrobots were demonstrated precise and controllable movements under low strength magnetic field. A system with a size of bacteria, capable to swim in viscous fluid in a controllable manner was satisfied basic principles for performing delicate tasks such as targeted drug delivery in medical application. Furthermore microrobots were advantaged from fabrications technology to make them biocompatible. In this study we reviewed a range of bio mimetic microrobots in terms of their design, fabrication, propulsion method in the fluid environment. The key characteristics of the helical shape microswimmers were optimised and the new design of helical microrobot is presented. The new design is demonstrated the microrobot with the variable pitch that is satisfied the fabrication requirement.

Three propulsion methods; Resistive Force Theory, Regularised Stokeslet Method and Slender Body Theory were implemented. The last two methods have not used before for remotely controlled microrobots. We provide the simulation platform for the swimming microrobot in a high viscose fluid. The simulation algorithm takes a desired velocity of microrobot and calculate the electric current is required to generate a dynamic magnetic field.

Chapter 1: Introduction

The potential use of microrobots in medical applications such as minimally invasive surgery has attracted scientists to work on designing microrobots [3]. Research into swimming microrobots showed two primary difficulties are the power source and suitable locomotion method, as there are many cells, proteins and fibres in biofluid that prevent the motion of the microrobots [15].

Artificial bacteria flagella is most popular microrobot was inspired by nature [18]. They have helical shape, are composed of magnetic material and are capable to mimic three-dimensional motion of the bacteria in a high viscous fluid.

Magnetically actuated helical micromachines can be used in a variety of biomedical applications such as cell characterisation, targeted drug delivery and in vivo diagnosis [14]. However, the issue of biocompatibility and the material used to make a microrobot needs to be considered carefully for in vivo application[18].

In addition, extremely small size of the microrobots and the complex biofluid environment make the design aspect very challenging. The design of microrobots depends on their application and the desired task. An overview of the main microrobot designs are summarised in the table 1.1. A few numbers of parameters has a key role on designing the helical shape microswimmer. Section 2.1 will demonstrated the details of the these effective parameters and optimise them to characterise the new design for helix shape microrobot.

The motivation for developing a simulation platform for microroswimmers navigation is raised to analyse their characteristic and behaviour under low magnetic field. Therefore, the major part of this project formed by analysing and implementing simulation methods which is described in section 2.3. The simulation challenge can be divided into main part; propulsion mechanism of the microrobot and actuation method. The popular method, Resistive Force Theory (RFT), describes the motion of the helix object in the low number regime is applied by most helical microswimmers's algorithms[18]. In this study, we implemented two more propulsion methods for the remotely controlled helical microswimmers in dynamic magnetic field. An actuation method of magnetic microrobot can be either force driven or torque driven [19]. Whilst the mechanism of both methods are explained in the section 2.3.2, we just implemented the torque driven actuation method in this study.

Fabrication of microdevice was a considerable challenge for a while [19] that has been overcome by fabrication methods such as 3D laser lithograph. Section 1.1.3 present a

brief history of fabrication techniques and section 2.2 describes the fabrication method is applied in this study.

In summery, the part of algorithms were developed for the propulsion mechanism of the microswimmers and actuation technique is based on Mahoney et al.'s research. The two new propulsion methods for the helical microswimmers were used in the Rodenborn et al.'s work which a reversible speed-variable motor such as micro metal gear motor helps to rotate microswimmer. In this study, applying those two propulsion mechanism on the microswimmers that are controlled remotely with magnetic field. Therefore, the algorithm is taken the desired translational velocity as an input and produce the rotational velocity as an output. By knowing the rotational velocity, we will be able to compute the electric current is required to produce the desired translational velocity. In addition, the new design is developed and printed for the helix which shows using variable pitch in helix design rather than constant pitch to satisfy the fabrication process. The result of all simulation is represented in the result chapter 3. Diagram 1.1 represents the structure of the project.

1.1 Literature review

1.1.1 Bioinspired microrobots

One of the most challenging aspects of designing a robot on a very small scale such as a nanorobot is simplicity. The reason is, integration between various components will become unfeasible on that scale if the design is complex. Hence the development of the nanorobot or even microrobot should be based on the essential functionality, avoiding any unnecessary components [4]. By learning from nature and mimicking the structure of live organisms, the successful scientific applications were created [19]. In the following section a few examples of swimming microrobots that were imitated from nature will describe.

Reynolds number To understand how micro organisms swim in a fluidic environment, it is essential to study their propulsion mechanism. In the fluidic regime the Reynold number (Re) has a substantial effect on a microdevice locomotion [14]. The Reynolds number describes the ratio of the inertial forces versus viscous forces according the following formula;

$$Re = \frac{UL\rho}{\mu} \quad (1.1)$$

Where U is velocity, L is characteristic length, ρ is the density and μ is viscosity of the fluid.

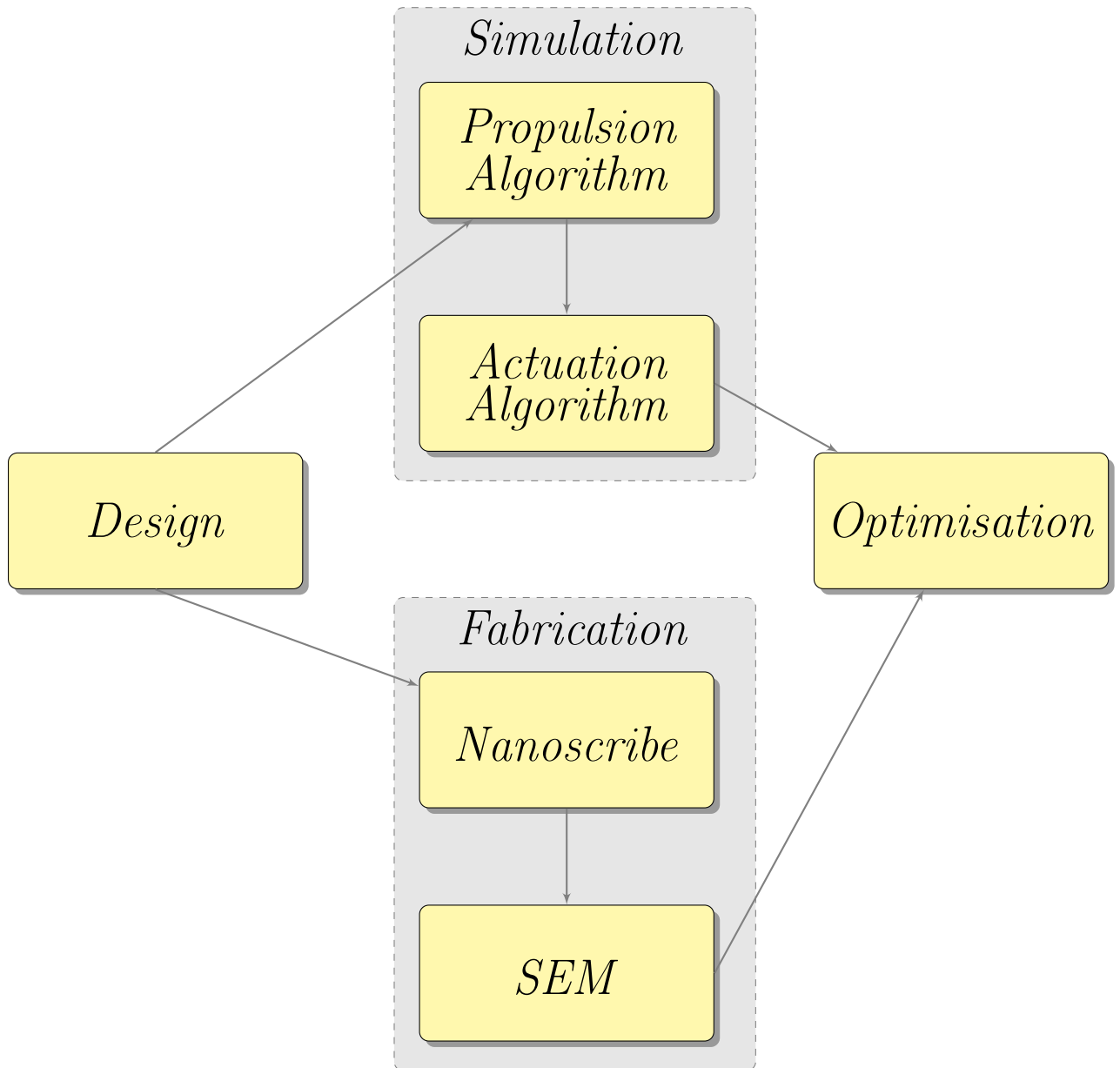


Figure 1.1: System Architecture.

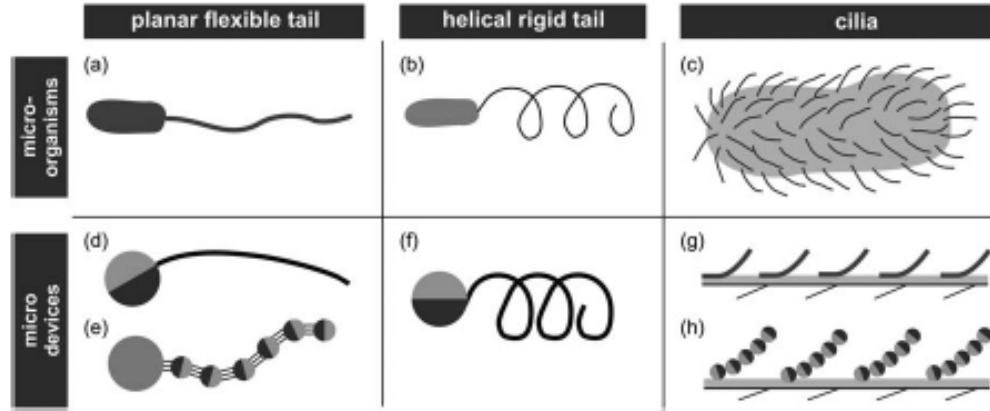


Figure 1.2: The illustration of both flagellum and cilia shapes and microdevices mimicked the flagellum and cilia structures. [15].

1.1.1.1 Flagella style microrobots

Helical flagella and cilia are two well-known microswimmers in nature that have had their functionality employed for motion generation in artificial microrobots (Figure 1.2) [4].

In 2007, Bell [4] presented the first artificial bacteria flagellum microrobots and then Zhang characterised them in 2009 [4]. This microrobot was formed of two components; a rigid helical tail and a soft magnetic metal head. The head diameter was $2.8\mu m$ and its length was $30 - 100\mu m$. Since then, other scientists proposed a slightly different design, that mostly have the rigid helical tail shape. However, in some cases the magnetic materials is used in the device tail rather than the head [4].

The helical rotation of flagella and the travelling wave beat of cilia are two non-reciprocal propulsion mechanisms in microorganisms. Mimicking a rotating flagellum at low Reynolds number to generate an adequate torque to overpower the high viscous drag requires two main elements; a rotary motor and a power source [19]. An electromagnetic rotary motor can be used in designing a helical flagella style microrobot that requires a considerable current. However piezoelectric rotary motors are an alternative option that are appropriate for miniaturisation but necessitate high input voltage. Hence, designing a microrobot with a combination of an onboard power source and a motor is a challenging task [19].

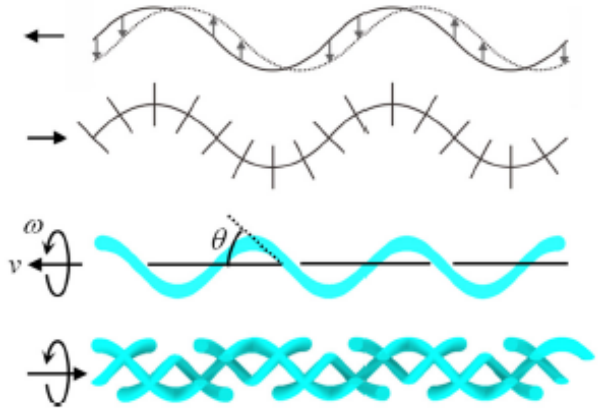


Figure 1.3: The propulsion mechanism of the smooth flagellum and a mastigonemes flagellum. The propulsion direction of smooth flagellum (top design) is opposite of flagella's propagation wave (second from the top). Their artificial design (blue structures) is based on their locomotion mechanism [4].

Another design of microswimmers was inspired by the function of magtigonemes in nature [22]. A smooth flagellum propels against the direction of the flagella's propagation wave. However, the flagellum covered by magtigoneme propels in the same direction as the flagellum wave (Figure 1.3). Mimicking the structure of flagellum and using 3D lithography and electron beam evaporation formed the fabrication method in these microswimmers. The anisotropic viscous drag on the flagella is an important fact for locomotion in low Reynolds number fluid. Flagella movement in the opposite direction of the flagella wave is because the viscous drag coefficient perpendicular to the flagella is greater than the viscous drag coefficient parallel to the flagella [22].

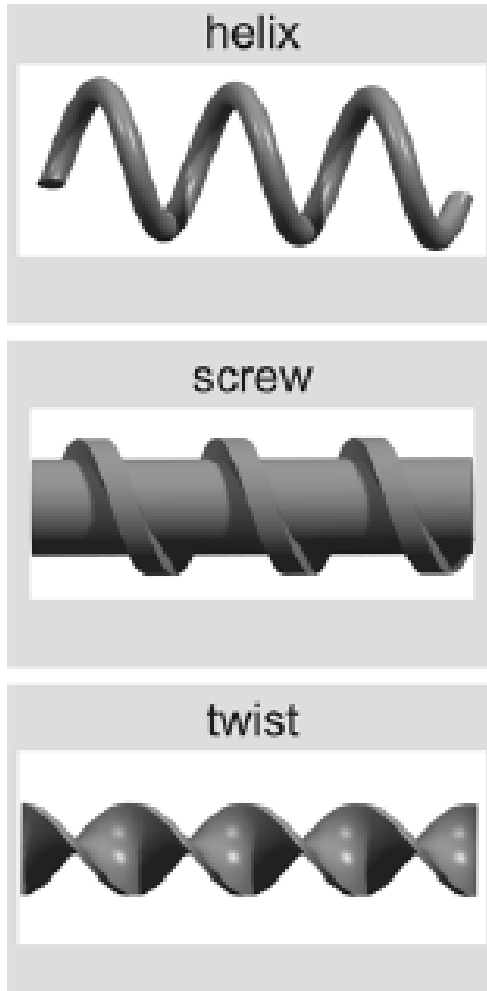


Figure 1.4: Three design of helical microswimmers [14].

The artificial smooth flagellum powered by an external magnetic field. The rotating field, i.e. rotational frequency, field strength and angles that defined the rotational axis is controlled by the current in the external coil. The helical microrobots rotate synchronously with the rotation of the magnetic field and move forward and backward accordingly [22]. The displacement of the microswimmer along the rotational axis can be measured and the result used to calculate the average velocity of the swimmers. There is a linear relationship between an input field frequency and swimming speed. According to their result [22], a propulsive force generated by the mastigoneme is in opposite direction of the force generated by the main helical filament. However, this velocity is only valid if the external force is zero. The proposed design [22] is rigid and an external stimulus may be used to regulate the swimming speed and direction if the swimmer can fold and unfold their structure.

There are three common shapes of micro-robots based on the rotary action; a helix, a screw and a twisted ribbon shape around its axis (Figure 1.4). For the purpose of drilling into solid matter such as biological tissue the screw and helix design would be more appropriate. The rotational motion

of helical micro swimmers is one of the most effective propulsion methods in the low Reynolds number scenarios because it leads to translational motion. Microrobots with the microspheres structure perform similarly to the helical swimmers and are capable of swimming in the flowing liquid within the microfluidic channel [5].

There are two main factors that affect the movements of the microrobot in the external magnetic field; **low coercivity and high saturation** magnetization. Also, the motion of the microrobot is related to its size given the same magnetic field strength and as such,

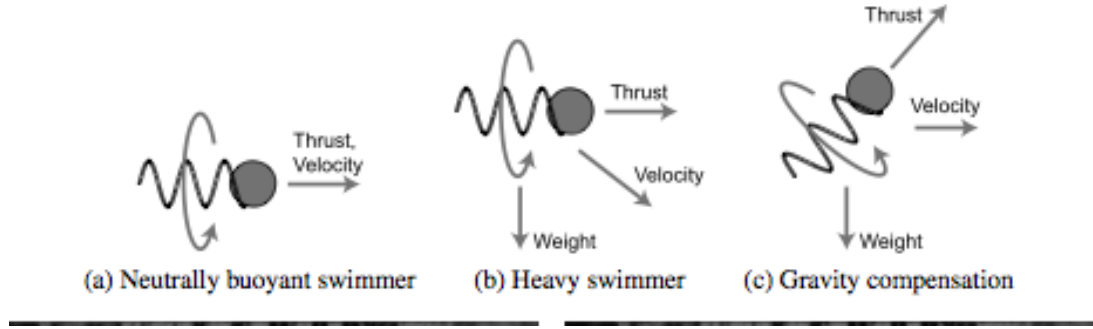


Figure 1.5: The effect of the gravity on the microrobot motion direction and gravity compensation [9].

by increasing the size of the microrobot with the inflexible magnetic material volume, the velocity will decrease [5]. The surface friction and the drag forces are two resistive forces that impede the microrobot's motion. Hence, the input magnetic force must be sufficient to overcome these forces for microrobot manipulation. Furthermore, the weight of the microrobot requires gravity compensation in the z-direction by the magnetic field. The navigation methodology should compensate for gravity to avoid sinking and enable velocity to be controlled wirelessly. Mahoney et al. described an algorithm for helical microswimmers velocity control plus gravity compensation. In the proposed model the correct pitch angle and rotation speed is calculated to achieve the commanded velocity (Figure 1.5).

A magnetic field can be used for controlling teams of microrobots as well as a single one. Kim et al. proposed a method that used a combination of two magnetic materials to attain on/off magnetization of each microrobot. The overall control of the group of microrobots was achieved by managing the magnetization state of each microrobot. In addition, a second technique has been developed for three-dimensional motion of the team of microrobots in a fluidic environment. In the latter method, each microrobot is designed in such a way that it uniquely responds to the input magnetic field. Therefore, several microrobots can provide feedback position control in 3D system [5]. An untethered spherical magnetic micromanipulator creates a locally induced rotational fluid flow gradient. The created rotational flow propels micro-objects in the flow area. A team of microrobots could perform a complex task in micro-transport and micro-assembly [5].

In another study [23], a helical microrobot was designed to swim in a low Reynolds number. Two designs are selected to run the experiment; the first one is a bare helical structure and the second one is the helical shape with the microholder attached at the end. Both designs will generate the corkscrew motion in a fluid environment when the magnetic field is about few mili Tesla. The second design (device with the microholder) is capable of transporting a microobject accurately to the target [23]. size and weight of the object

In Tottori et al.'s study eight designs of microrobots were proposed and tested. The uniform static magnetic field was used to explore the magnetic shape anisotropy and the magnetic actuation was monitored in the rotating magnetic field. In the static magnetic field the set of microrobots had helical angles θ ranging from 45° to 70° when suspended in the deionised water.

This showed (Figure 1.6) that a smaller helix angle θ results in a less misalignment angle α because microrobots longest axes will be aligned to the direction of the external magnetic field. However in helical micro-robot with larger helix angles (θ), the magnetization direction would change to the radial axes of the helix [23]. In the rotating magnetic field, the micro helical swimmer exhibits different behaviours depending on the strength of the applied frequency in the fixed magnetic field. At low frequencies the micro helix oscillated around the helical axes, however the oscillating behaviour changed to the corkscrew motion after increasing the applied frequency in the magnetic field. This is similar to characteristics of microrobots with an incorporated micro-holder [23].

The velocity of helical micro swimmers depends on their size and shape. A linear relationship was observed between the input frequencies and swimming velocity of the micro swimmers. The outcome of the comparison between three microhelixes with the same helix angles showed that the microhelix with the greatest diameter has the highest speed, in accordance with the following formula;

$$U = \frac{(C_n - C_1) \sin \theta \cos \theta}{2(C_n \sin^2 \theta + C_1 \cos^2 \theta)} (d\varpi) \quad (1.2)$$

Where C_n is a drag coefficient perpendicular to the filament and C_1 is a drag coefficient parallel to the filament. ϖ is the rotational frequency and d is the rotational diameter of the helix [23].

The important role of helix angle in the magnetization structure of helical micro swimmers was confirmed by Peyer et al. [13], who used direct laser writing (DLW) as a fabrication method on a Magnetic Polymer Composite (MPC). The MPC are non-cytotoxic and showed super paramagnetic characteristic because magnetic material was already included in the polymer.

The relationship between the torque T , the drag force F , the object's velocity ν and rotational speed ω is linear and modelled by 6×6 resistant matrix as below;

$$\begin{bmatrix} F \\ T \end{bmatrix} = \begin{bmatrix} A & B \\ C & D \end{bmatrix} \begin{bmatrix} \nu \\ \omega \end{bmatrix}$$

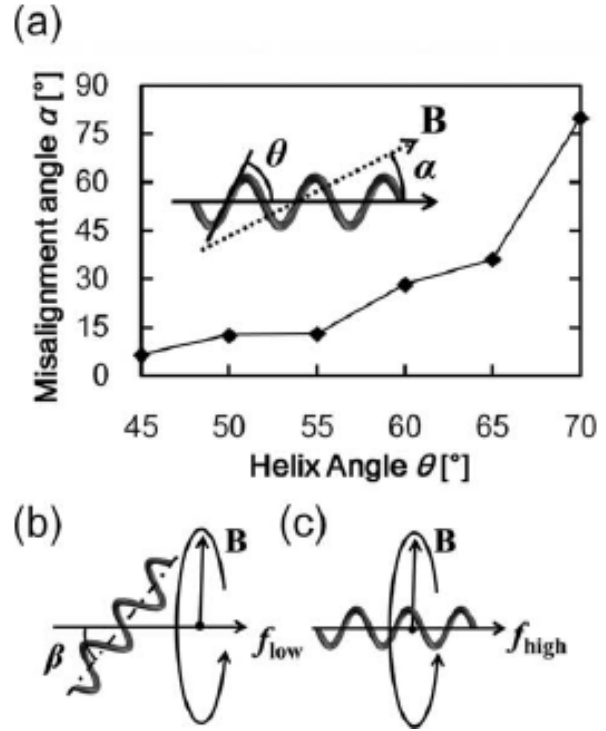


Figure 1.6: (a) The misalignment of helical angle α with different helix angle (b) the oscillation behaviour of the microswimmer with the high and low frequencies [23].

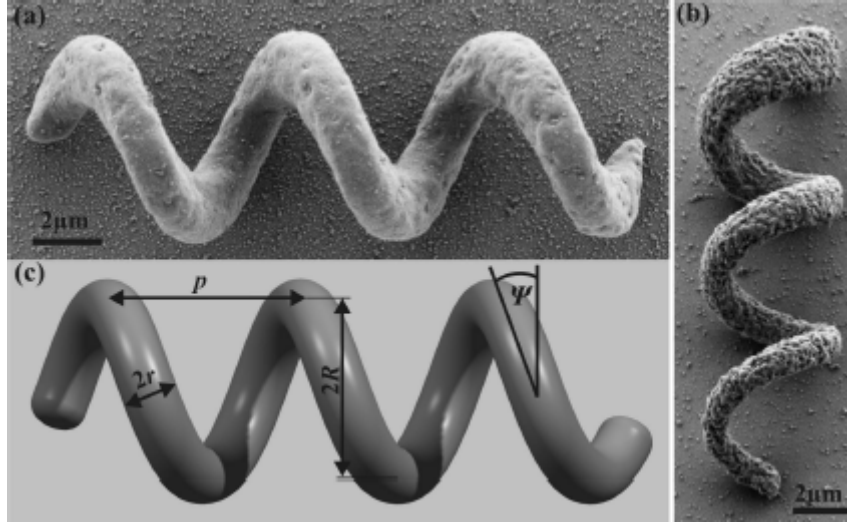


Figure 1.7: The prototype of microhelical device. (a) Scanning electron microscopic image of the micro polymer composite with the 2 vol.% nanoparticle fill factor and (b) 4 vol.% of nanoparticle fill factor. (c) The CAD model shows all the parameters required for the microhelical design [13].

Where A , B and D are matrices 3×3 and only depend on the object's geometry and fluid velocity. In the study performed by Purcell [16] has been proved matrices B and C are equal ($B = C$) for a typical flagellum. There are few methods in use to model the resistance matrices and low Reynolds flow such as the method of regularized stokeslets, the boundary element method and the method of fundamental solution. In designing a microrobot the main parameters required to concentrate on are the helicity angle ψ , the helix radius R , the pitch p and the filament radius r as illustrated in Figure 1.7 part (c).

Magnetic actuated microrobot is divided into two categories; torque driven microrobot and force driven microrobots. The micro robot using the torque-driven method is more favourable than the force-driven method because their rotation is based on applying torque rather than a force to pull the device [13].

Another approach for powering a micro robot is using the catalytic conversion of chemical energy into mechanical energy (Figure 1.8). In this method, the catalyst accelerates the consumption of hydrogen peroxide and helps the self-propulsion of micro robot to pump the fluid to transport cells and colloidal particles [27]. The catalytic tube is fabricated with a sub micrometer diameter. This technique is not applicable for the minimally invasive surgery (MIS) yet because the catalytic material used

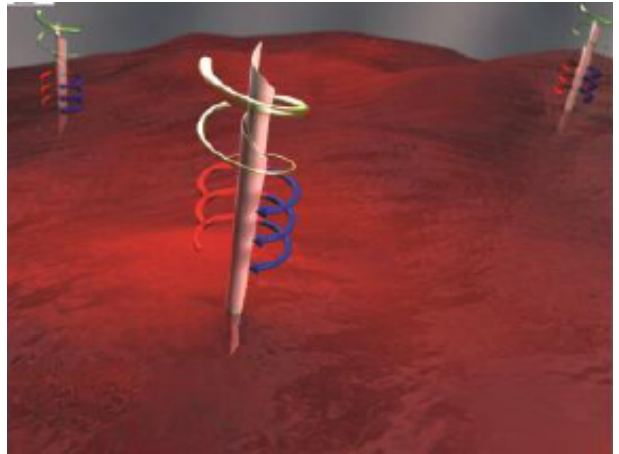


Figure 1.8: Demonstrating the drilling motion of the nanotubes under rotating magnetic field [27].

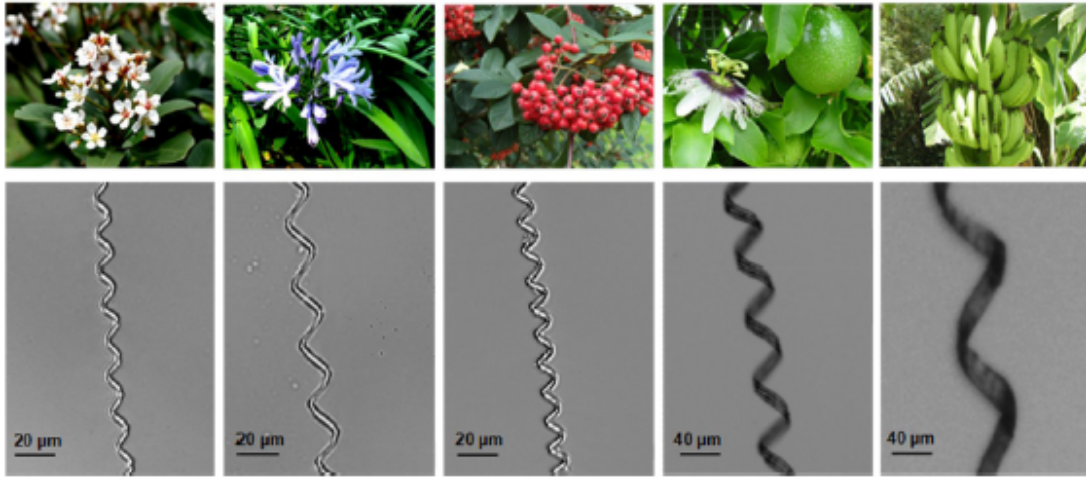


Figure 1.9: The shape of the Xylem in different plants . [9].

in the fabrication process of nanotubes is toxic. Hence, biocompatible fuel is required to be developed in order to apply this technique in a live cell environment [27].

Alternatively, the micro driller can be powered and controlled by using an external magnetic field such that changes in the frequency of the rotating magnetic field switch the rotational orientation of the micro tool from the horizontal position to the vertical one. The vertical orientation of the rolled up microtube and its sharp helical design makes the device suitable for drilling into biological tissue. In addition, the micro driller can be used for targeted drug delivery in MIS [27].

1.1.1.2 Plant-based microrobots

The helical microstructures are not limited to having flagellum-like structures and microrobots with general cilia-like feature have been designed. Gao et al. observed the helical microstructures that imitates spiral water-conducting vessels of different plants.

In order to obtain unstretched spiral vessel several plants were collected and their leaves were macerated and washed with pure water. Tweezers were used to uncover compressed spiral vessels in the planar networks. Leaves were gently scored and two segments were pulled apart to a permanent length to stretch the spiral vessels. These spiral vessels were kept in a glass slide and covered with a thin layer (20nm) of titanium and nickel (80nm) using an E-beam evaporator [9]. The helical vessels were coated in nail polish and baked for 2 minutes to impound the helix and protect the structure. The final product is a photoresist film on glass that was cut into required lengths.

The fabrication process involves coating isolated spiral xylem vessel plant fibres within a (Figure 1.7) thin magnetic layer. Xylem tissue transports the plant's required food such as water and other nutrition from the root to the leaves using capillary action [9]. Use of plant material in this method enables simple three-dimensional microswimmers fabrication and biocompatibility. In addition, the magnetic cover helps to ensure accurate directional control and high-speed propulsion. Therefore the fabrication processes were extremely simplified as the main component of the helical microswimmers is from nature and more than a million individual micro helicals can be made from a very small section of the

plant stalk [9]. Using mechanical stretching can control geometric variables of the helical vessels such as the pitch and helix angle and hence plenty of helical microswimmers can be reproduced. The final shape of the helical microswimmer is determined mainly by the initial diameter of the unstretched spiral vessel. The process of stretching helical plant structure was performed via plastic deformation so that the number of helical turns are constant and tensile stretching of the plant fibre stretching is negligible [9].

The method used for precise propulsion control and characterising the locomotion behaviour of the plant-based microswimmers is similar to the method applied in Gao et al. study.

According to Gao et al. [4] experiment, the plant-based microswimmers exhibited high speed movement ($85 \mu m$) in raw biological medium such as pure human serum under the rotating magnetic field. However, their swimming speed in pure water ($90 \mu m$) was slightly higher than human serum. Hence, an increased velocity of the biological fluid has a minor effect on the plant-driven microswimmers, which is an important advantage of this microdevice over the common microrobots

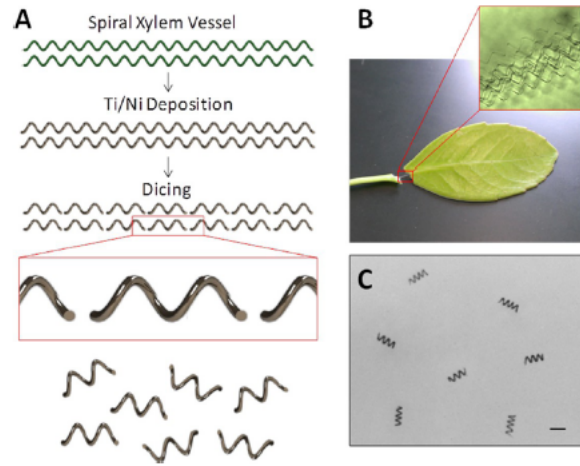


Figure 1.10: (A) The stages were required to make a plant-based microrobot. (B) A microscopic image of the a xylem helical structure [4].

1.1.2 Actuation methods

The bacteria inspired (Page 5) [15]

1.1.3 Fabrication methods

Historically, the fabrication of the microrobot was the main problem that recent fabrication methods offer a feasible solution [4]. In 2007, the first artificial bacteria flagella was fabricated based on thin-film deposition and self-scrolling methods [18]. In this method. They used InGaAs/GaAs bilayer for fabricating helical tail and Ni for actuation microrobot's head. The similar fabrication method employed by Zhang in 2009 with the addition of a Cr layer between the microrobots' tail and its head [18]. An improved adhesion of microrobot was the result of adding Cr layer.

3D laser direct writing (DLW) and electron beam decomposition are methods used since then. A typical fabrication process consists of two stages. Initially the core structure of the artificial helical microswimmer is printed using 3D lithography and then electron beam evaporation is used for ferromagnetic thin film coating [22]. Performance of each microswimmer (with different design) can be imaged by the scanning electron microscope (SEM). After the fabrication process is completed, the next step is to release the structure into deionised water using the tungsten probe. The tank with deionised water is installed in the middle of the three-axis Helmholtz setup.

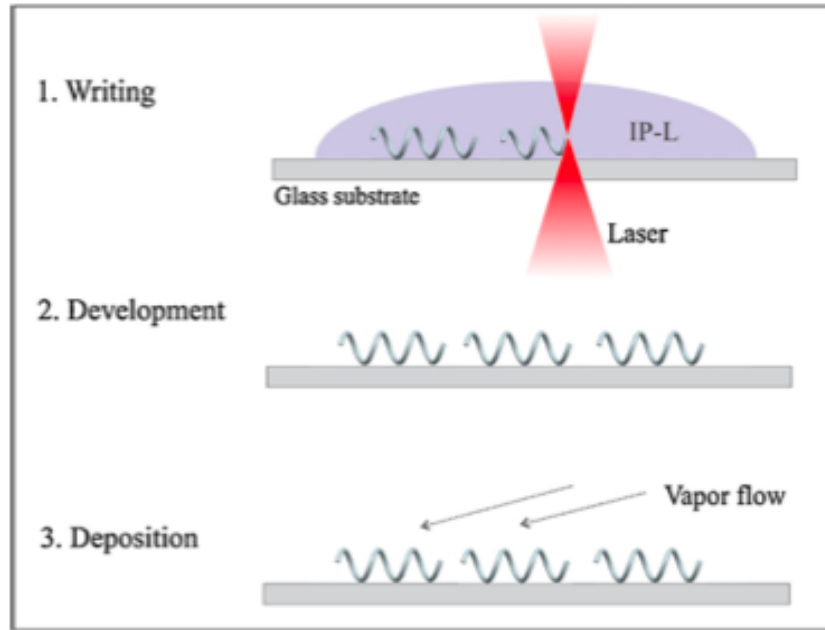


Figure 1.11: DLW steps. step 1 is writting helical microrobots, in step 2 microrobots were developed in isopropyl alcohol and step 3 is coating them by a layer of Ni and Ti. [17].

To improve biocompatibility for in-vivo applications, the microrobot can be covered with a thin layer of titanium. In addition, the microrobot's structure was layered with nickel for the purpose of magnetic actuation.

Qiu et al. [17] reported a successful application of helical microrobots for drug delivery were known as “smart” drug carriers. Again, they used DLW for the fabrication method as shown in the Figure 1.11.

The smart drug carriers were coated in a layer of temperature-sensitive liposomes which is composed of a lipid bilayer and was proposed for cancer therapy in local hyperthermia treatments [17]. The main component of temperature-sensitive liposomes is Dipalmitoylphosphatidylcholine (DPPC) which transforms from solid to liquid gel at the 41°C and released encapsulated drugs.

Qiu et al. [18] were used commercially available material such as ORMOCOMP for fabrication of helical microrobots in their recent experiment. ORMOCOMP is a bio-compatible photoresist which can improve the potential use of microrobots for in vivo applications becuase it supports viability, cell proliferation and normal morphology of various cell lines. For the purpose of magnetic microrobot actuation, soft magnetic material such as Fe, Ni and Co are commonly used in microscale structures. The main reason is their biocompatibility with surface decomposition methods, however Ni and Co are cytotoxic and pure iron can be biodegradable [18]. ORMOCOMP helical swimmers were coated onto a thin layer of Fe (25nm) using electron beam decomposition.




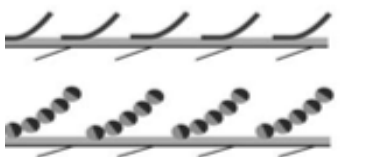
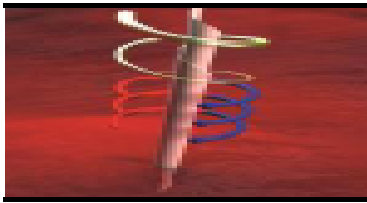


Microrobot Image	Design	Fabrication Method	propulsion method	Citation
	<ul style="list-style-type: none"> • Helical Screw Shape 	<ul style="list-style-type: none"> • Direct Laser Writting (DLW) • Two-photon Polymerization 	<ul style="list-style-type: none"> • RFT 	<ul style="list-style-type: none"> • [14]
	<ul style="list-style-type: none"> • Helical rigid tail 	<ul style="list-style-type: none"> • Direct Laser Writting (DLW) • Two-photon Polymerization 	<ul style="list-style-type: none"> • RFT 	<ul style="list-style-type: none"> • [15]
	<ul style="list-style-type: none"> • Planar flexible tail 	<ul style="list-style-type: none"> • The EMA coil system 	<ul style="list-style-type: none"> • SBT • RFT 	<ul style="list-style-type: none"> • [5]
	<ul style="list-style-type: none"> • Cilia 	<ul style="list-style-type: none"> • The EMA coil system 	<ul style="list-style-type: none"> • SBT 	<ul style="list-style-type: none"> • [5]
	<ul style="list-style-type: none"> • Nanotube 	<ul style="list-style-type: none"> • Molecular Beam Epitaxy (MBE) 		<ul style="list-style-type: none"> • [27]
	<ul style="list-style-type: none"> • Plant-based 	<ul style="list-style-type: none"> • Macerating Plant's Leaves • Seperating Spiral Vessels • Stretching spiral Vessels • Coating with Ti 		<ul style="list-style-type: none"> • [4]
	<ul style="list-style-type: none"> • Jellyfish 	<ul style="list-style-type: none"> • The EMA coil system 		<ul style="list-style-type: none"> • [6]

Table 1.1: Different types of microrobots and their fabrication method.

Chapter 2: Methods

2.1 Microrobot design

Novel part of design using microrobot with the variable pitch to enable it vertically fabricated.

Author	Shape	Length	Pitch	Pitch-angle	Radius	Filament-radius	Speed
Arcene		1000	1000	1000	1000	1000	1000
Dexter	Sparse	20000	1000	1000	1000	1000	1000
Dorothea	Sparse	10000	1000	1000	1000	1000	1000

Table 2.1: Microrobot's design comparisons

2.2 Microrobot fabrication

The main challenge of the fabrication process is not just fabricating the extremely small object. There are number of other factors that need to be considered to select an appropriate approach for fabricating helical shape microrobot. An ideal fabrication approach should have control over design parameters and in particular it should be suitable for applying magnetic material for the actuation purpose [15].

The complete fabrication process is summarised in the diagram 2.1. The process started by importing the structure files into the software called Describe for the pre-processing purpose. The structures file contains all the microrobots that is designed by the software called Solidwork. The next stage is writing the structure using nanoscribe facility, which is done in the clean room. After few hours, the structures will be ready and they can be seen under the SEM. However, the structure made of polymer and the pictures of non-metal object under the SEM is not perfect. Thus the polymer made microrobot were coated with the layer of metal (usually gold) first, this process called sputtering coating process. At this stage, the picture of microrobot were analysed under the SEM and if they are satisfactory, they will go to the final stage which is magnetization process. However, we never try the magnetization stage in this project because the aim was to optimise the structures in terms of design and fabrication and there was no plan to run an experiment within the short period of time. The pictures were encountered to have a problem were sent to the design stage for further optimisation process. In the following two sections,

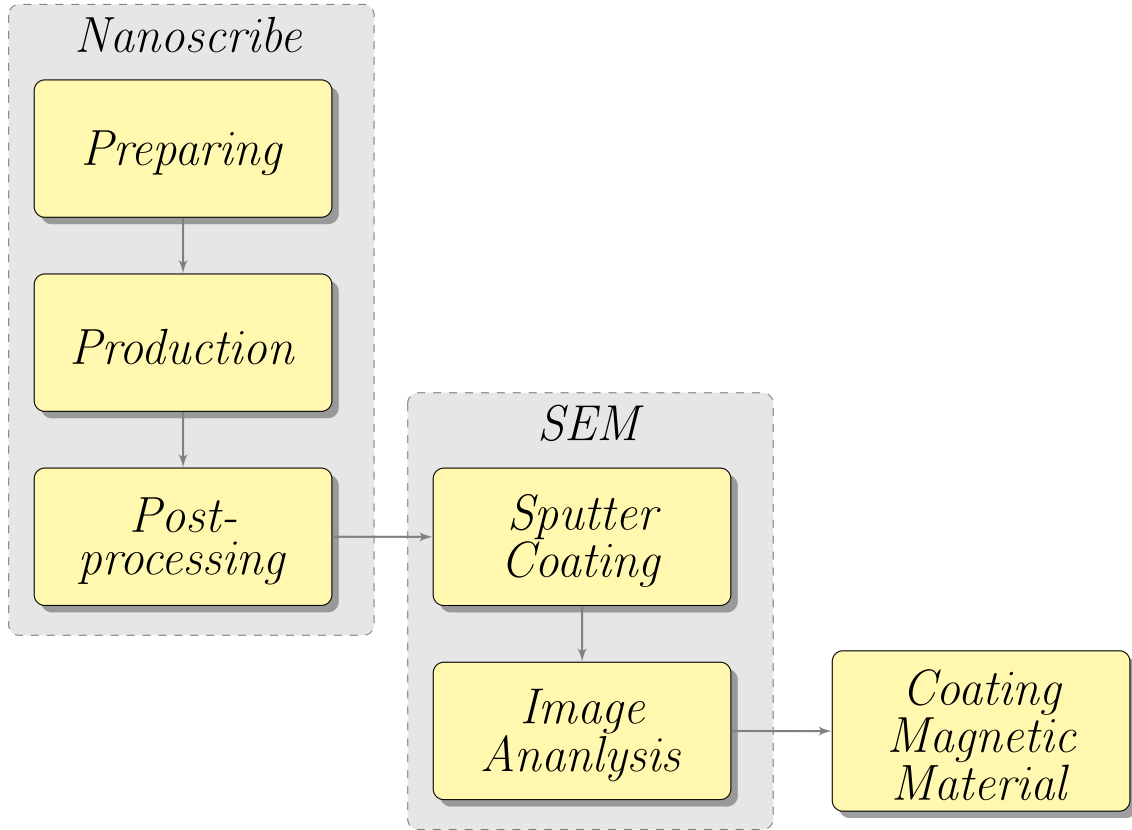


Figure 2.1: Fabrication diagram. The nanoscribe technology is employed for the fabrication process and it followed by analysing structure under SEM. The final stage (yellow block in third column) has not been tried in this project.

we will explain the mechanism of the two photon lithography technique and SEM in more details.

2.2.1 Nanoscribe

Nanoscribe is the company provide sophisticated system and device for true 3D micro and nanofabrication. Their system is based on the laser lithography and it used two-photo polymerization technique for the fabrication. The fabrication device combines two modes for writing; the high-speed galvo-mode and an ultra-precise piezo-mode. The former is for fastest fabrication and it makes the structure in a layer-by-layer process. The latter is mainly for printing arbitrary 3D trajectories [12]. The complete nanoscribe package made of three components, Photonic Professional GT, the software and IP Photoresists. Photosensitive material is used in both modes for structuring arbitrary 3D patterns in a high-resolution. The properties of the photosensitive material, the laser power and the size of the spot in the material are determined the voxel size. Extremely small voxel size can be achieved when focusing optics is used with a high numerical aperture. The fabrication process in each mode is based on moving the voxel relative to the sample. The galvo mode approach is called Moving-beam Fixed-sample (MBFS) which the laser beam is scanned galvanometric mirrors and piezo-actuators will control the vertical movement. However in piezo-mode, piezo actuators is moving the substrate in all three dimensions

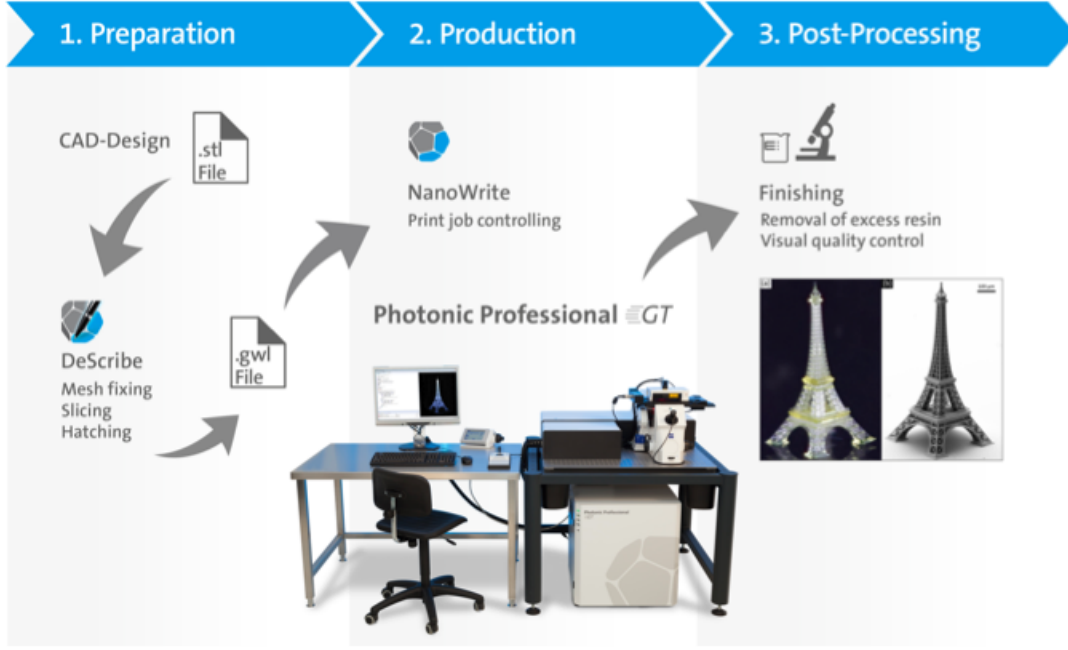


Figure 2.2: nanoscribe workflow. The stages are involved in 3D micro-printing with nanoscribe device is shown in the diagram [12].

to achieve highly precise focus trajectory. This type of implementation is known as Fixed-beam Moving-sample (FBMS) [12].

The whole process of fabrication is formed of three stages; preparation, production and post-processing. In the first stage, the STereoLithography (stl) file that contains the design of structures will import into the software tool called DeScribe. In this software, each design will go through three steps for fixing the mesh, slicing and hatching. By completing these three steps, the result will be the General Writing Language (gwl) format file that is ready for the production stage. The production is the stage for controlling the print job that has been done by user-friendly graphical interface software, NanoWrite. This software controls different aspects of the lithography system such as autofocus, exposure dose and substrate positioning. The final stage is removing the excess resin to improve the visual quality [12].

IP Photoresists is a high viscous fluid that comes as part of nanoscribe package. It is used to maximise the performance of the multiphoton polymerization process. It has high mechanical stability and sticks to different substrates very well [12]. A wide range of materials with different mechanical, optical or chemical properties can be used for the substrate in direct laser writing. The choice of the substrate material is application dependent. For example, in optical applications, transparent materials such as glass are more appropriate. In the latter application, the substrate is mainly for supporting the polymer structures. Also, we can use pre-structured substrates such as transparent microfluidic chips that polymer structures can be printed on the substrate. In that case, the functionality of multiphoton lithography can be improved by combining the mechanical parts with the substrate [12].

In this project we used nanoscribe device to print microswimmers using the galvo-mode of the machine. The whole printing unit is located in the clean room¹. The fabricated structures were observed under the SEM and all the images result will be presented and discussed in the result 3 and discussion chapters 4 respectively.

2.2.2 Scanning Electron Microscope (SEM)

SEM is a powerful device for obtaining high magnification images to analyse and examine the material or individual features. SEM is invented 50 years ago and it is used extensively in diverse scientific fields such as biology, medicine or metallurgy, to name just a few. The SEM can provide images with the high-resolution down to 25 Angstroms.²

SEM generates a range of signals at the surface of solid specimens by using a focused beam of high-energy electrons. The process is started from producing electron beam by the electron gun at the top of the microscope and then travels into the microscope. The microscope is placed in the vacuum. Then the beam focused down into the specimen by passing through the electromagnetic fields and lenses. Once the focused electron beam interacts with the specimen, electrons are revealed from the specimen. At this point, the back-scattered electrons are collected by the detectors and were converted into variety of signals. Ultimately, generated signals sent to the screen to form the final image of the specimen[24].

The key advantages of using SEM over traditional microscope is having a large depth of field and also higher resolution. In addition, researchers has more control over the degree of magnification because SEM uses electromagnets[24].

We need to prepared samples before using the SEM because it using the electron in the vacuum condition. That means sample should not contain any water otherwise the water will vaporise in the vacuum. This is high-vacuum SEM. If we require an image of a wet sample such as biological specimen we can use the low-vacuum SEM. In that case, the specimen chamber contains air that avoid dehydrating of samples. Because the produced

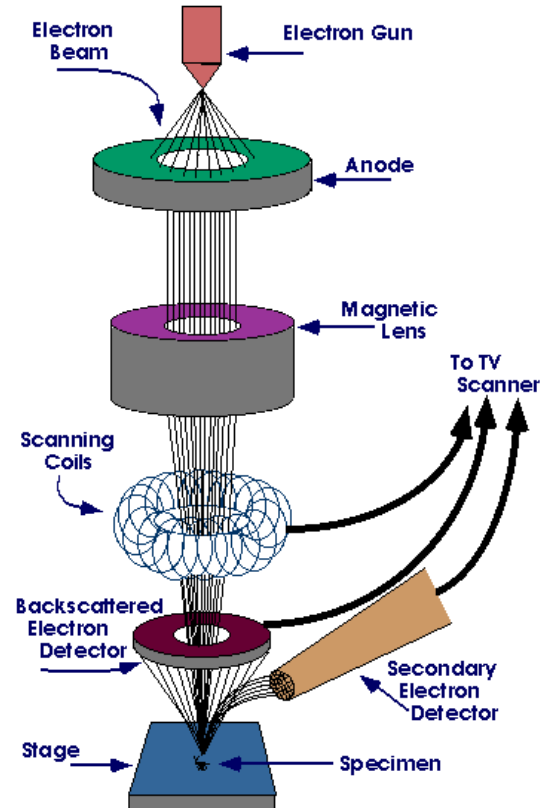


Figure 2.3: Scanning Electron Microscop. The components of the SEM is shown in the diagram [24].

¹Clean room is an environment with controlled concentration of airborne particle to make it suitable for product manufacturing [10].

²1 Angstrom = 1.0×10^{-10} Metres

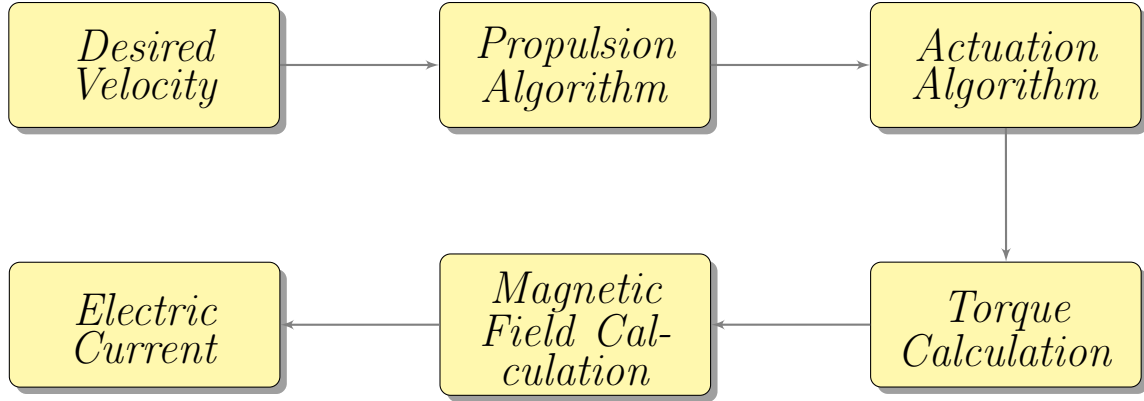


Figure 2.4: Simulation algorithm. The main components of implementing the simulation is shown in the diagram.

images are based on the electron-sample interaction, if the sample is made of non-metal material, the final image is not very clear. Thus, they need to be covered by a metal to make it conductive. The process of covering the sample with metal is called sputter coating[24].

sputter coating In the sputter coater, there is small chamber in the vacuum to place the sample in. An electric field and argon gas used in order to release the electron from the argon and convert it into positive charged atom. Then, argon ions and negatively charged gold foil are attracted to each other and as a result gold atoms fall from the surface of the gold and settle onto the surface of the specimen. Therefore a thin gold layer covers the surface of the sample and make it conductive for SEM machine[24].

In this project, the microrobot structure is made of polymer and we made them conductive by applying the sputter coating process and then analysed them under SEM. The images of the microrobot structures before and after coating is presented in the result section 3. In the following section, the simulation of microrobot is demonestareted in detail.

2.3 Simulation

The simulation of the microrobot is formed by two main components; helical microrobot propulsion mechanism and actuation method. The complete algorithm that describes the implementation of the simulation system is represented in the diagram 2.4. In this algorithm, the desired velocity is given to the system and the required electric current to make the dynamic magnetic field will be an output. The pseudocode of the algorithm 1 is provided more details in each step of the implementation and the complete computation is explained in section 2.3.1.2 and section 2.3.2.

Data: Velocity (\mathbf{V}), RFT, RSM, SBT
while $\mathbf{V} \neq 0$ **do**
 Select propulsion method from (RFT, RSM, SBT);
 Compute propulsion matrix coefficient (b, c);
 Decompose \mathbf{V} to \mathbf{V}_{hor} and \mathbf{V}_{ver} ;
 if $\|\mathbf{V}_{hor}\| = 0$ **then**
 Rotational velocity $\Omega = \frac{\|\mathbf{V}\| + d_{11}\|\mathbf{f}\|}{e_{11}}$;
 Microrobot direction point $\tilde{\mathbf{X}} = -\hat{\mathbf{g}}$;
 Go to next step
 else
 Rotational velocity $\Omega = \frac{\|\tilde{\mathbf{V}}\| \cos(\psi) + d_{11}\|\mathbf{f}\| \cos(\psi - \alpha)}{e_{11}}$;
 Microrobot direction point $\tilde{\mathbf{X}} = \frac{\tilde{\mathbf{V}}}{\|\tilde{\mathbf{V}}\|}$;
 Go to next step;
 end
 Compute Torque $\tau = b\mathbf{V} + \Omega c$;
 Compute Magnetic field \mathbf{B} from $\tau = \mathbf{V}M \times \mathbf{B}$;
 Compute Electric current i from $|\mathbf{B}| = (\frac{b^2}{(b^2 + l^2)^{3/2}})\mu_0 i$
end

Algorithm 1: Simulation algorithm

2.3.1 Modeling helical propulsion

Analysing fluid dynamic phenomena on microorganism is a fundamental approach to model microorganism locomotion [21].

A helical bacterial flagellum can be used as a reference to model a helical microrobot. The essential parameters to model a helix are, helix length (L), pitch (λ), pitch angle (θ), radius (R), filament radius (a) and contour length ($\Lambda = L/\cos\theta$). Figure 2.5 shows the helix parameters evidently [20]. The flagella parameters were measured for several species of bacteria and its result showed the helical pitch is typically ranging between $2R$ and $11R$, ($2R < \lambda < 11R$). Also the helix length (L) varies from 3λ to 11λ , ($3\lambda < L < 11\lambda$).

The flagella rotation at low Reynolds number exerts an axial thrust (F) and torque (T) related to the rotation rate (ω) and flagellum axial velocity (ν). At the same time, fluids was exerted the force ($-F$) and the torque ($-T$) on the swimming microrobots [16]. The fluid dynamic govern by the Stokes equations (2.1) in the low Reynolds regime;

$$-\nabla p + \eta \nabla^2 \nu = 0 \quad (2.1)$$

Where η and p are fluid dynamic velocity and pressure respectively. Therefore thrust (F) and torque (T) are linearly related to the ν and ω as there are no derivation of time in the equations 2.1. Thses linear relationship can be defined as follow;

$$F = A\nu + B\omega \quad (2.2)$$

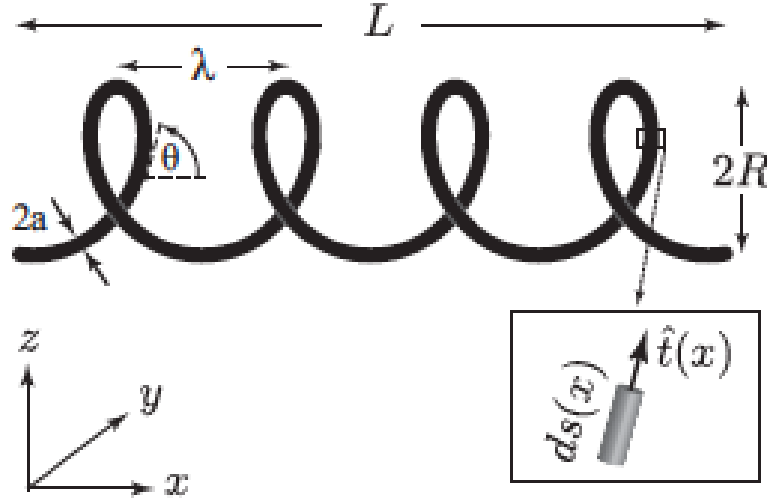


Figure 2.5: The essential helix parameters to design a helical microrobot [20].

$$T = C\nu + D\omega \quad (2.3)$$

Therefore, a matrix $\begin{pmatrix} A & B \\ C & D \end{pmatrix}$ defined as propulsion matrix the model to explain the flagellar swimming motion described by following equation [20] as mentioned in the literature review earlier;

$$\begin{bmatrix} F \\ T \end{bmatrix} = \begin{bmatrix} A & B \\ C & D \end{bmatrix} \begin{bmatrix} \nu \\ \omega \end{bmatrix}$$

The elements in the symmetric 2×2 matrix (propulsive matrix) in the above equation only depends on flagellum geometry. The propulsive matrix elements can be computed by three methods called; resistive force theory, slender body theory and regularized Stokeslet theory which are described in details in sections 2.3.1.1, 2.3.1.4 and 2.3.1.3 respectively.

2.3.1.1 Resistive force theory for microrobot with two degree of freedom

The swimming velocity and efficiency of the microrobot can be predicted by Resistive force theory (RFT) [16]. The force exerted on the fluid by micro swimmer were calculated initially and the micro swimmer will have a net movement if the force is not zero [11]. Furthermore, the swimming velocity will decrease if the helical body attached to the inert head. Figure 2.7 shows an arbitrary filament motion which is defined by $s(l, t)$. A direction of the helix velocity (U) is along x-axis and its rotation is symmetric about the x-axis. The following assumption has been made in order to use the RFT.

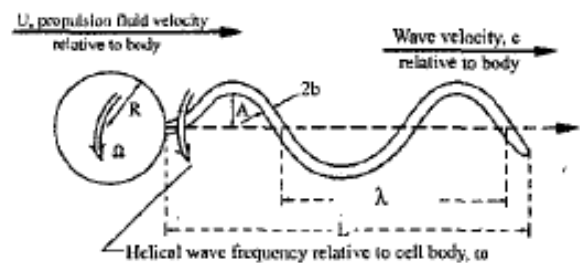


Figure 2.6: [3].

The geometry of the helix is on the yz -plane and it always attached to the robot body (can be a sphere). The filament motion is periodic and filament length is constant at all the time. Acceleration can be neglected as the system is in the low Re number fluid. Hence, the equations 2.4 and 2.5 will describe the force balance and the moment balance in the x -axis direction. The thrust and torque will be determined by integrating over the first term of the force balance and moment balance equations (2.4 and 2.5) respectively [3].

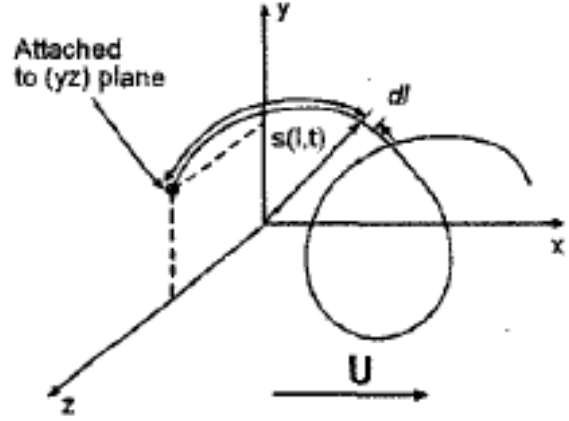


Figure 2.7: A motion of an arbitrary filament [3].

$$\frac{1}{\Delta T} \int_0^{\Delta T} \int_0^L f_x(l, t) dl dt + C_D U = 0 \quad (2.4)$$

$$\frac{1}{\Delta T} \int_0^{\Delta T} \int_0^L [\mathbf{r} \times \mathbf{f}(l, t)] \cdot \mathbf{e}_1 dl dt + C_{D\Omega} \Omega = 0 \quad (2.5)$$

Where ΔT is the time filament motion repeats and integration is taken over the whole length (L) of the helix.

In order to solve the integration problem, the force (f) is required to be defined. Therefore, a new coordination system was introduced and the force vector was defined as a composition of force per unit length in the normal and tangent directions. Two identical motions are considered for the swimming microrobots are; rotating and translating (assumed in the x -axis direction). Hence, the force balance and moment balance equations are simplified as following;

$$N f_x L + C_D U = 0 \quad (2.6)$$

$$N f_y A L + C_{D\Omega} \Omega = 0 \quad (2.7)$$

Where N and A are number of filaments and helical amplitude of filaments respectively. Also f_x and f_y shows the components of the force vector along x and y directions. In addition, C_D and $C_{D\Omega}$ were computed by equations 2.8 and 2.9 where R is radius of the helix and μ is fluid velocity.

$$C_D = 6\pi\mu R \quad (2.8)$$

$$C_{D\Omega} = 8\pi\mu R^3 \quad (2.9)$$

The f_x and f_y are written as composite of forces in the normal and tangent directions;

$$f_x = f_t \cos \theta - f_n \sin \theta \quad (2.10)$$

$$f_y = f_t \sin \theta + f_n \cos \theta \quad (2.11)$$

$$\tan \theta = \frac{\lambda}{2\pi A} \quad (2.12)$$

$$f_t = -C_t(U \cos \theta - \omega A \sin \theta) \quad (2.13)$$

$$f_n = -C_n(-U \sin \theta - \omega A \cos \theta) \quad (2.14)$$

Where C_t and C_n called resistance coefficients [3];

$$C_t = \frac{2\pi\mu}{\ln\left(\frac{2\lambda}{b}\right) - \frac{1}{2}} \quad (2.15)$$

$$C_n = \frac{4\pi\mu}{\ln\left(\frac{2\lambda}{b}\right) + \frac{1}{2}} \quad (2.16)$$

Microrobot's swimming speed and rotation rate were determined by solving the equations 2.13 and 2.14. Therefore, thrust (F), torque (T) and drag (D) on flagellum can be predict by following equations [20];

$$F = (\Omega R)(C_n - C_t) \sin \theta \cos \theta \frac{L}{\cos \theta} \quad (2.17)$$

$$T = (\Omega R^2)(C_n \cos^2 \theta + C_t \sin^2 \theta) \frac{L}{\cos \theta} \quad (2.18)$$

$$D = U(C_n \sin^2 \theta + C_t \cos^2 \theta) \frac{L}{\cos \theta} \quad (2.19)$$

Finally, the efficiency of the helical swimmers can be computed as follow;

$$efficiency = \frac{FU}{T\omega} \quad (2.20)$$

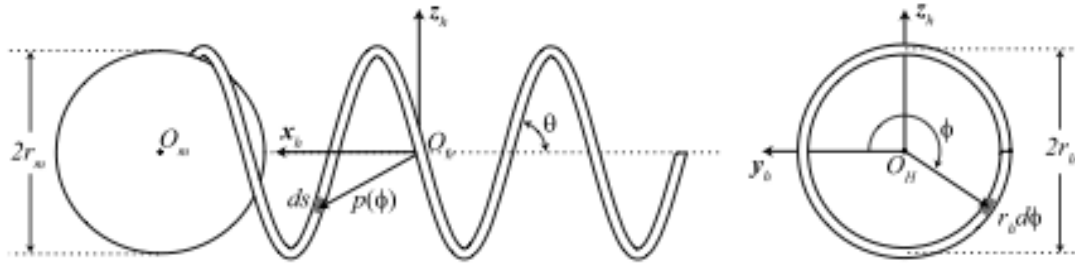


Figure 2.8: Three dimation configuration for the helical microrobot with a magnetic spherical head. The origin of the helix coordinate is denoted with \mathbf{O}_h and \mathbf{x}_h is the central axis of the helix [9].

2.3.1.2 Resistive force theory for six degree of freedom

The two degree of freedom microrobot (one dimation model) with RFT was exhibited a successful result [9] for studying the helical microswimmers. However, complex motion of swimming microrobot could not be explained in one dimation model. Therefore, the RFT was needed to be implemented in three dimation model which means defining a microrobot with six degree of freedom. The microrobot's is used in this model has a helical tail with the shpere head attached to it as shown in 2.8.

The RFT is applied with the assumption that the force and torue is applied on the helical tail and sphear head are independent. Therefore, the force f_h and torque τ_h of the helical tail are obtained by RFT and f_m and τ_m are force and torue are applied on the sphear head respectively. The equation 2.98 is the summation of two forces and torques which is the total force and torque.

$$\mathbf{f} = \mathbf{f}_h + \mathbf{f}_m \quad \tau = \tau_h + \tau_m \quad (2.21)$$

According to the RFT the force on the extremely teeny segment of the helix is defined by the segment velocity and drag forces acts on that segment. First RFT takes the veloity (\mathbf{V}_s) was applied on the small length of helix and decompound it into two vectors, one parallel (\mathbf{V}_{\parallel}) and one perpendicular (\mathbf{V}_{\perp}) to that segment. Also, the drag force is acting on that small length decomposed into two vectors; parallel (ξ_{\parallel}) and perpendicular (ξ_{\perp}) to that segment. Therefore, the force is applied on the small segment is formulated as follow;

$$d\mathbf{f}_{\perp} = \xi_{\perp} \mathbf{V}_{\perp} ds \quad (2.22)$$

$$d\mathbf{f}_{\parallel} = \xi_{\parallel} \mathbf{V}_{\parallel} ds \quad (2.23)$$

Where ξ_{\parallel} and ξ_{\perp} are drag coefficients and they have been approximated by number of scientists emprically. The fluidic force (\mathbf{f}_h) acts on the helix is computed by integrating over these differential forces along the helix length. Because the integration is performed in three dimation we need to define two seperate coordinate frame, one for the given

differential segment (frame s) and one for the helix (frame h). The helix pitch angle (θ) and radius (r_h) is used to define the geometry of the helix with the assumption that the central axe of the helix is parallel to the \mathbf{x}_h . Figure 2.8 presents the helix coordinate origin (O_h) with its three axis ($\mathbf{x}_h, \mathbf{y}_h, \mathbf{z}_h$). The helix is represented in a cylindrical coordinate³

system with the polar angle ϕ . Each vector in the segment frame (s) can be written in the helix frame (h) by applying a rotation matrix as shown in the equation 2.25;

$${}^h\mathbf{R}_s(\phi) = \mathbf{R}_x(\phi)\mathbf{R}_y(-\theta) \quad (2.25)$$

Where $\mathbf{R}_x(\phi)$ is rotation of a vector in the segment frame (s) with the ϕ angle with respect to the x axis and then will apply $\mathbf{R}_y(-\theta)$ which rotate the result vector with the $(-\theta)$ angle with respect to the y axis. The final result is a vector in the helix (h) frame 2.26.

$${}^h\mathbf{P}(\phi) = \begin{bmatrix} \frac{r}{\tan(\theta)} & r \cos(\phi) & r \sin(\phi) \end{bmatrix} \quad (2.26)$$

Hence, as appears in the equation 2.27 the differential relating velocity to force can be shown with respect to the frame of a random segment along the helix in the segment frame in three dimention.

$${}^s d\mathbf{f}_s = {}^s\mathbf{\Xi} {}^s\mathbf{V}_s ds \quad (2.27)$$

$${}^s\mathbf{\Xi} = \begin{bmatrix} \xi_{\parallel} & 0 & 0 \\ 0 & \xi_{\perp} & 0 \\ 0 & 0 & \xi_{\perp} \end{bmatrix} \quad (2.28)$$

In the equation 2.27 the force ${}^s\mathbf{f}_s$ and velocity ${}^s\mathbf{V}_s$ of the segment is represented in the segment's own frame. In the segment frame, the x_s axis is assumed to be parallel to that segment and two other axis (y_s, z_s) are perpendicular to that segment as we can see in the 2.28. Hence, the relationship between forces and velocity can be expressed in the helix frame (2.29) by using the drag coefficient unity matrix 2.28.

$${}^h d\mathbf{f}_s = {}^h\mathbf{\Xi}(\phi) {}^h\mathbf{V}_s ds \quad (2.29)$$

where

$${}^h\mathbf{\Xi}(\phi) = {}^h\mathbf{R}_s(\phi) {}^s\mathbf{\Xi} {}^s\mathbf{R}_h(\phi) \quad (2.30)$$

³The cylindrical coordinate is an extention of the polar coordinate to the three dimention space. It defines based on the radius r , the angle θ and the z coordinate such that the following equation are valid

$$x = r \cos \theta \quad y = r \sin \theta \quad z = z \quad (2.24)$$

The velocity of the small helix segment \mathbf{V}_s is formed of the rotational helix velocity ($\boldsymbol{\omega}$) and its translational velocity (\mathbf{V}). The summation of two velocities is described in the equations 2.31.

$$\mathbf{V}_s = \mathbf{V} + \boldsymbol{\omega} \times \mathbf{P}(\phi) = \mathbf{V} - \mathbf{P}(\phi) \times \boldsymbol{\omega} \quad (2.31)$$

The equation 2.31 is the velocity of the segment in the segment frame. This equation can be written with respect of the helix frame, as shown below;

$${}^h\mathbf{V}_s = {}^h\mathbf{V} - \Delta\{{}^h\mathbf{P}(\phi)\}^h\boldsymbol{\omega} = {}^h\mathbf{V} + \Delta\{{}^h\mathbf{P}(\phi)\}^{Th}\boldsymbol{\omega} \quad (2.32)$$

where the vector cross product ($\mathbf{P}(\phi) \times \boldsymbol{\omega}$) can be represented in the form of skew-symmetric matrix ⁴ $\Delta\{{}^h\mathbf{P}(\phi)\}^h$ and a vector $\boldsymbol{\omega}$:

$$\mathbf{P}(\phi) \times \boldsymbol{\omega} = \Delta\{{}^h\mathbf{P}(\phi)\}^h\boldsymbol{\omega} \quad (2.33)$$

And according to the skew-symmetric matrix property we have:

$$-\Delta\{{}^h\mathbf{P}(\phi)\}^h = \Delta\{{}^h\mathbf{P}(\phi)\}^{Th} \quad (2.34)$$

After substituting 2.32 into 2.29:

$${}^hd\mathbf{f}_s = {}^h\boldsymbol{\Xi}(\phi){}^h\mathbf{V}ds + {}^h\boldsymbol{\Xi}(\phi)\Delta\{{}^h\mathbf{P}(\phi)\}^{Th}\boldsymbol{\omega}ds \quad (2.35)$$

The equation 2.35 manifests the relation between differential force and translation and rotation velocity of the small helix segment in the helix frame. Each force is applied on an infinitesimally small section of helix generates a torque around helix centre. As a result the relation between the force and torque at an arbitrary slice of helix (using parameter ϕ) can be represented in the helix frame:

$${}^hd\boldsymbol{\tau}_s = {}^h\mathbf{P}(\phi) \times {}^hd\mathbf{f}_s = \Delta\{{}^h\mathbf{P}(\phi)\}^h d\mathbf{f}_s \quad (2.36)$$

Therefore the total fluidic torque and force of the helix can be figured out by integrating the small torques and forces that applied on the infinitesimally segments of the helix along the helix length:

$$\mathbf{f}_h = \int d\mathbf{f}_s \quad \boldsymbol{\tau}_h = \int d\boldsymbol{\tau}_s \quad (2.37)$$

The final torque and force can be obtained from the equations 2.98 by integrating with respect to the polar angle ϕ . As it been seen in the figure 2.8 the ds can be written with respect with the polar angle ϕ as follow:

⁴In mathematics, a square matrix A is called a skew-symmetric if its transpose is equal to its negative ($A^T = -A$).

$$ds = \frac{r_h d\phi}{\sin(\theta)} \quad (2.38)$$

after substituting the 2.35 into 2.36 and replacing ds with the equation 2.38 we have the following equations which is integrating with respect with ϕ from $-\pi n$ to πn for an n turn helix;

$$\begin{aligned} {}^h\mathbf{f}_h = & \left(\frac{r_h}{\sin(\theta)} \int_{-\pi n}^{\pi n} {}^h\Xi(\phi) d(\phi) \right) {}^h\mathbf{V} \\ & + \left(\frac{r_h}{\sin(\theta)} \int_{-\pi n}^{\pi n} {}^h\Xi(\phi) \Delta\{{}^h\mathbf{P}(\phi)\}^T d(\phi) \right) {}^h\boldsymbol{\omega} \end{aligned} \quad (2.39)$$

$$\begin{aligned} {}^h\boldsymbol{\tau}_h = & \left(\frac{r_h}{\sin(\theta)} \int_{-\pi n}^{\pi n} \Delta\{{}^h\mathbf{P}(\phi)\} {}^h\Xi(\phi) d(\phi) \right) {}^h\mathbf{V} \\ & + \left(\frac{r_h}{\sin(\theta)} \int_{-\pi n}^{\pi n} \Delta\{{}^h\mathbf{P}(\phi)\} {}^h\Xi(\phi) \Delta\{{}^h\mathbf{P}(\phi)\}^T d(\phi) \right) {}^h\boldsymbol{\omega} \end{aligned} \quad (2.40)$$

Computing all four integrals in the eqations 2.39 and 2.40 will result in two equations that is expressed force (${}^h\mathbf{f}_h$) and torque (${}^h\boldsymbol{\tau}_h$) in terms of the angular (${}^h\boldsymbol{\omega}$) and translational velocity (${}^h\mathbf{V}$):

$$\begin{bmatrix} {}^h\mathbf{f}_h \\ {}^h\boldsymbol{\tau}_h \end{bmatrix} = \begin{bmatrix} {}^h\mathbf{A}_h & {}^h\mathbf{B}_h \\ {}^h\mathbf{C}_h & {}^h\mathbf{D}_h \end{bmatrix} \begin{bmatrix} {}^h\mathbf{V}_h \\ {}^h\boldsymbol{\omega} \end{bmatrix}$$

Where ${}^h\mathbf{A}_h$, ${}^h\mathbf{B}_h$ and ${}^h\mathbf{C}_h$ are:

$${}^h\mathbf{A}_h = \begin{bmatrix} a_{h11} & 0 & 0 \\ 0 & a_{h22} & 0 \\ 0 & 0 & a_{h22} \end{bmatrix} \quad (2.41)$$

$${}^h\mathbf{B}_h = \begin{bmatrix} b_{h11} & 0 & b_{h13} \\ 0 & b_{h22} & 0 \\ 0 & 0 & b_{h33} \end{bmatrix} \quad (2.42)$$

$${}^h\mathbf{C}_h = \begin{bmatrix} c_{h11} & 0 & c_{h13} \\ 0 & c_{h22} & 0 \\ c_{h13} & 0 & c_{h33} \end{bmatrix} \quad (2.43)$$

and each matrix element will calculate by following eqations:

$$a_{h11} = \frac{2\pi n r_h (\xi_{\parallel} \cos^2(\theta) + \xi_{\perp} \sin^2(\theta))}{\sin(\theta)} \quad (2.44)$$

$$a_{h11} = \frac{\pi n r_h (\xi_{\perp} + \xi_{\perp} \cos^2(\theta) + \xi_{\parallel} \sin^2(\theta))}{\sin(\theta)} \quad (2.45)$$

$$b_{h11} = 2\pi n r_h^2 (\xi_{\parallel} - \xi_{\perp}) \cos(\theta) \quad (2.46)$$

$$a_{h13} = \frac{-2\pi n r_h^2 (\xi_{\parallel} - \xi_{\perp}) \cos(\theta)}{\tan(\theta)} \quad (2.47)$$

$$a_{h22} = \frac{-3\pi n r_h^2 (\xi_{\parallel} - \xi_{\perp}) \cos(\theta)}{2} \quad (2.48)$$

$$a_{h33} = \frac{-\pi n r_h^2 (\xi_{\parallel} - \xi_{\perp}) \cos(\theta)}{2} \quad (2.49)$$

$$c_{h11} = \frac{2\pi n r_h^3 (\xi_{\perp} \cos^2(\theta) + \xi_{\parallel} \sin^2(\theta))}{\sin(\theta)} \quad (2.50)$$

$$c_{h11} = \frac{-2\pi n r_h^3 (\xi_{\perp} \cos^2(\theta) + \xi_{\parallel} \sin^2(\theta))}{\sin(\theta) \tan(\theta)} \quad (2.51)$$

$$\begin{aligned} c_{h22} = & \frac{2\pi n r_h^3 (\xi_{\parallel} \cos^2(\theta) + \xi_{\perp} \sin^2(\theta) - \xi_{\perp}/2)}{\sin(\theta)} \\ & + \frac{\pi n r_h^3 (\xi_{\parallel} \cos^2(\theta) - \xi_{\perp} \sin^2(\theta) - \xi_{\perp})}{2 \tan^2(\theta) \sin(\theta)} \\ & + \frac{(\pi n r_h)^3 (\xi_{\parallel} \cos^2(\theta) - \xi_{\perp} \sin^2(\theta) + \xi_{\perp})}{3 \tan^2(\theta) \sin(\theta)} \end{aligned} \quad (2.52)$$

$$\begin{aligned} c_{h33} = & \frac{\pi n r_h^3 \xi_{\perp}}{\sin(\theta)} - \frac{\pi n r_h^3 (\xi_{\perp} \cos^2(\theta) + \xi_{\parallel} \sin^2(\theta) - \xi_{\perp})}{2 \tan^2(\theta) \sin(\theta)} \\ & + \frac{(\pi n r_h)^3 (\xi_{\perp} \cos^2(\theta) + \xi_{\parallel} \sin^2(\theta) + \xi_{\perp})}{3 \tan^2(\theta) \sin(\theta)} \end{aligned} \quad (2.53)$$

We assumed the fluidic torque and force are applied on microrobot by helical tail is independent from the spherical head. We define a vector \mathbf{K} such that it connects the centre of the helix \mathbf{O}_h to the centre of the spherical magnetic head \mathbf{O}_m as shown in the Figure 2.8. The well-known equations for the rotational and translational drag coefficient of the sphere particle in the stokes flow are [26]:

$$\xi_{vm} = 6\pi\eta r_m \quad \xi_{\omega m} = 8\pi\eta r_m^3 \quad (2.54)$$

Where η is the fluid viscosity and r is the radius of the sphere. A magnet velocity is produced by an arbitrary movement of the microswimmer and can be expressed in the helix frame as the product of the head's velocity and translational drag coefficient:

$${}^h\mathbf{V}_m = {}^h\mathbf{V} + {}^h\boldsymbol{\omega} \times {}^h\mathbf{K} = {}^h\mathbf{V} - {}^h\mathbf{K} \times {}^h\boldsymbol{\omega} = {}^h\mathbf{V} + \Delta\{{}^h\mathbf{K}\}^{Th}\boldsymbol{\omega} \quad (2.55)$$

Also, force on the spherical magnet is the product of the translational and rotational force:

$${}^h\mathbf{f}_m = \xi_{vm} {}^h\mathbf{V} + \xi_{vm} \Delta\{{}^h\mathbf{K}\}^{Th}\boldsymbol{\omega} \quad (2.56)$$

The force acts at the arm \mathbf{K} and the drag is generated by the rotation of the spherical magnet will cause a drag torque by magnet head:

$${}^h\boldsymbol{\tau}_m = {}^h\mathbf{K} \times {}^h\mathbf{f}_m + \xi_{\omega m} {}^h\boldsymbol{\omega} \quad (2.57)$$

After replacing ${}^h\mathbf{f}_m$ with 2.56 and using screw-symmetric matrix instead of cross-product, the final torque for magnetic head will be:

$${}^h\boldsymbol{\tau}_m = \xi_{vm} \Delta\{{}^h\mathbf{K}\} {}^h\mathbf{V} + (\xi_{vm} \Delta\{{}^h\mathbf{K}\} \Delta\{{}^h\mathbf{K}\}^T + \xi_{\omega m} \mathbf{I}) {}^h\boldsymbol{\omega} \quad (2.58)$$

We can write the equation ?? in terms of matrices;

$${}^h\mathbf{A}_m = \xi_{vm} \mathbf{I} \quad {}^h\mathbf{B}_m = \xi_{vm} \Delta\{{}^h\mathbf{K}\}^T \quad {}^h\mathbf{C}_m = \xi_{vm} \Delta\{{}^h\mathbf{K}\} \Delta\{{}^h\mathbf{K}\}^T + \xi_{\omega m} \mathbf{I} \quad (2.59)$$

Therefore, the total torque (${}^h\boldsymbol{\tau} = {}^h\boldsymbol{\tau}_h + {}^h\boldsymbol{\tau}_m$) and force (${}^h\mathbf{f} = {}^h\mathbf{f}_h + {}^h\mathbf{f}_m$) applied on microswimmer are:

$$\begin{bmatrix} {}^h\mathbf{f} \\ {}^h\boldsymbol{\tau} \end{bmatrix} = \begin{bmatrix} {}^h\mathbf{A} & {}^h\mathbf{B} \\ {}^h\mathbf{B}^T & {}^h\mathbf{C} \end{bmatrix} \begin{bmatrix} {}^h\mathbf{V} \\ {}^h\boldsymbol{\omega} \end{bmatrix}$$

By replacing the matrices with their equivalent;

$$\begin{bmatrix} {}^h\mathbf{f} \\ {}^h\boldsymbol{\tau} \end{bmatrix} = \begin{bmatrix} {}^h\mathbf{A}_h + {}^h\mathbf{A}_m & {}^h\mathbf{B}_h + {}^h\mathbf{B}_m \\ ({}^h\mathbf{B}_h + {}^h\mathbf{B}_m)^T & {}^h\mathbf{C}_h + {}^h\mathbf{C}_m \end{bmatrix} \begin{bmatrix} {}^h\mathbf{V} \\ {}^h\boldsymbol{\omega} \end{bmatrix}$$

$${}^h\mathbf{A} = \begin{bmatrix} a_{11} & 0 & 0 \\ 0 & a_{22} & 0 \\ 0 & 0 & a_{22} \end{bmatrix} = \begin{bmatrix} a_{h11} + \xi_{vm} & 0 & 0 \\ 0 & a_{h22} + \xi_{vm} & 0 \\ 0 & 0 & a_{h22} + \xi_{vm} \end{bmatrix} \quad (2.60)$$

$${}^h\mathbf{B} = \begin{bmatrix} b_{11} & 0 & b_{13} \\ 0 & b_{22} & b_{23} \\ 0 & -b_{23} & b_{33} \end{bmatrix} = \begin{bmatrix} b_{h11} & 0 & b_{h13} \\ 0 & b_{h22} & \xi_{vm} |\mathbf{K}| \\ 0 & -\xi_{vm} |\mathbf{K}| & b_{h33} \end{bmatrix} \quad (2.61)$$

$${}^h\mathbf{C} = \begin{bmatrix} c_{11} & 0 & c_{h13} \\ 0 & c_{22} & 0 \\ c_{h13} & 0 & c_{33} \end{bmatrix} = \begin{bmatrix} c_{h11} + \xi_{\omega m} & 0 & c_{h13} \\ 0 & c_{h22} + \xi_{vm}|\mathbf{K}|^2 + \xi_{\omega m} & 0 \\ c_{h13} & 0 & c_{h33} + \xi_{vm}|\mathbf{K}|^2 + \xi_{\omega m} \end{bmatrix} \quad (2.62)$$

Hence, the total nonfluidic force (\mathbf{f}) which produced as a result of gravity and total non-fluidic torque ($\boldsymbol{\tau}$) generated by magnetic field. Then, the next algorithm is implemented to control velocity of the microrobot with considering gravity will detail in ??.

2.3.1.3 Regularized Stokeslet method

A regularization parameter can be used as a proxy for the body radius to minimise numerical errors in modelling a flagellum as a one dimensional filament in a low Reynolds [21]. number fluids. The Regularized Stokeslet method (RSM) is one of the approach to solve the zero Reynolds number linear ‘Stokes flow’ equations;

$$\left. \begin{aligned} 0 &= -\nabla p + \mu \nabla^2 u + f \\ 0 &= \nabla \cdot u \end{aligned} \right\} \quad \text{Stokes flow equations} \quad (2.63)$$

where u (velocity), p (pressure), μ (kinematic viscosity), and f (force) are measured per unit volume. The singular ‘Stokeslet’ solution for the equations 2.63 corresponds to the purely viscous component (point force) of the flow which was determined by moving sphere. The ‘Stokeslet’ solution for unit force acts in the j -direction and concentrated at $\boldsymbol{\xi}$, where f is;

$$f(x) = \delta(x - \boldsymbol{\xi})e_j \quad (2.64)$$

$\delta(x - \boldsymbol{\xi})$ is called Dirac delta distribution. The velocity in the i -direction driven by this force is defined as follow;

$$S_{ij}(\mathbf{x}, \boldsymbol{\xi}) = \left(\frac{\delta_{ij}}{r} + \frac{r_i r_j}{r^3} \right) \quad (2.65)$$

Where δ_{ij} denotes Kronecker delta tensor, $r_i = x_i - \xi_i$ and $r^2 = |\mathbf{x} - \boldsymbol{\xi}|^2 = r_1^2 + r_2^2 + r_3^2$. The flow concentrates at point $\boldsymbol{\xi}$ by the force \mathbf{F} where $\mathbf{f}(\mathbf{x}) = \delta(\mathbf{x} - \boldsymbol{\xi})\mathbf{F}$. The solution is given by finding the velocity $u_i(\mathbf{x})$;

$$u_i(x) = \left(\frac{1}{8\pi\mu} \right) S_{ij}(\mathbf{x}, \boldsymbol{\xi}) F_j \quad (2.66)$$

The RFT and SBT for modelling of flagellum driven flow were formed on the base of the Stokeslet [21]. These methods solved the three dimensional flow problem with flexible boundaries without using direct computation for the differential equations. Therefore, the provided solution are extremely efficient in terms of computational costs. The fluid velocity was modeled by the following equation;

$$\mathbf{u}(\mathbf{x}) = \left(\frac{1}{8\pi\mu}\right) \int_S \mathbf{f}(\boldsymbol{\xi}) \cdot \mathbf{S}(\mathbf{x}, \boldsymbol{\xi}) dS_\xi \quad (2.67)$$

Where S is a collection of lines or surfaces of flagella, $\mathbf{f}(\boldsymbol{\xi})$ shows force per unit length or area. $\mathbf{f}(\boldsymbol{\xi})dS_\xi$ denotes the force flagella body exerted on the fluid and $-\mathbf{f}(\boldsymbol{\xi})dS_\xi$ is the force fluid applies to the body. The flagella is represented by equation 2.67 with the boundary S and parameter $\boldsymbol{\xi}(\mathbf{s})$ where $0 < s < 1$ is scaled arclength parameter. However, the flow field at any point $\mathbf{x} = \boldsymbol{\xi}(s)$ is singular and the collection of points on the surface of the filament are required to calculate the force per unit length. The collection of points were replaced on a small distance from the centreline;

$$\mathbf{X}(\mathbf{s}_q) = \boldsymbol{\xi}(s_q) + a(s_q)\mathbf{n}(s_q) \quad (2.68)$$

where $a(s_q)$ is a radius of slender body and $\mathbf{n}(s_q)$ is a unit normal vector. Point distributions of Stokeslets at any point $\mathbf{x} = \boldsymbol{\xi}_q$ and line distribution inside the notional surface of the flagella are both singular. However, surface distributions of Stokeslets do not result in singular velocity but it still require attentive numerical implementations [21]. The ‘regularized Stokeslet’ introduced an exact solution for the equations ?? to overcome these issues. This method used a cut off function (ψ) with a regularization parameter (ϵ) to smooth point forces such that $\int_{R^3} \psi_\epsilon(\mathbf{x}) dV_x = 1$.

$$\left. \begin{aligned} 0 &= -\nabla p + \mu \nabla^2 \mathbf{u} + \mathbf{f} \psi_\epsilon(\mathbf{x} - \boldsymbol{\xi}), \\ 0 &= \nabla \cdot \mathbf{u} \end{aligned} \right\} \quad \text{Stokes flow equations with regularization parameter} \quad (2.69)$$

In RSM method, with a assumption of $\psi_\epsilon(\mathbf{x} - \boldsymbol{\xi}) := 15\epsilon^4/8\pi\mu r_\epsilon^7$ and $r_\epsilon = \sqrt{r^2 + \epsilon^2}$ the regularized Stokeslet velocity tensor measured by the the following:

$$S_{ij}^\epsilon(\mathbf{x}, \boldsymbol{\xi}) = \frac{\delta_{ij}(r^2 + 2\epsilon^2) + r_i r_j}{r_\epsilon^3} \quad (2.70)$$

Therefore the boundary for intergal equation (2.71) is defined and the fluid velocity at location \mathbf{x} is;

$$\mathbf{u}(\mathbf{x}) = \left(\frac{1}{8\pi\mu}\right) \int_S \mathbf{f}(\boldsymbol{\xi}) \cdot \mathbf{S}^\epsilon(\mathbf{x}, \boldsymbol{\xi}) dS_\xi \quad (2.71)$$

Where

2.3.1.4 Slender body theory

Slender body theory represents the helix body with an arrangement of doublets and Stokeslets along the filament central line (Figure 2.9). This theory represented by Lighthill for the first time and was followed by Johnson with some modification. According to Lighthill there is some distance q from any given point on the helix body such that q

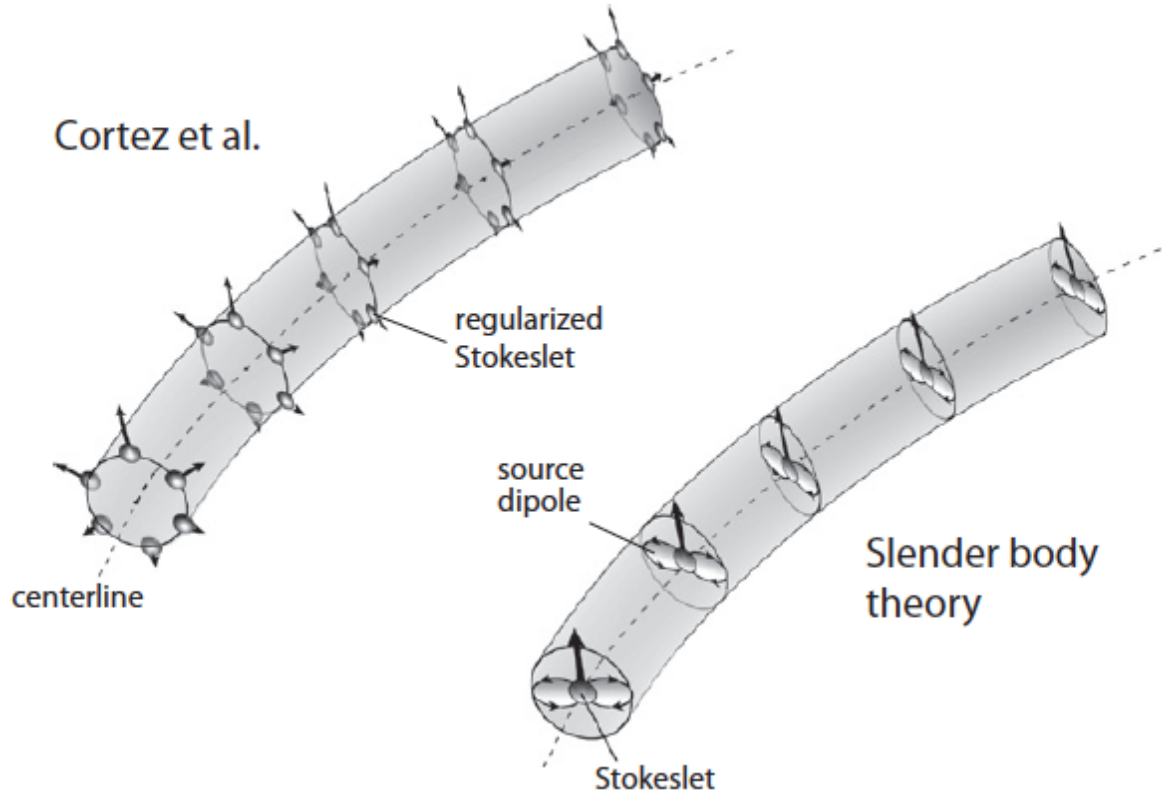


Figure 2.9: RSM and SBT. In RSM the surface of helix filament separated by cross-sectional segmentation and each surface represents by Stokeslets (left image). In the SBT, the Stokeslets are arranged along the central filament line (right image) [20].

is between the radius of the filament a and helix pitch λ . The dipoles in this distance are important to determine the flow at the given point. He proved for the induced fluid flow on the given segment the sum of near-field and far-field solutions could be made independent of any distance (q) by defining the dipoles as follows;

$$-\frac{a^2 \mathbf{f}_\perp(s)}{4\mu} \quad (2.72)$$

Where s is a location along the central axis of the filament and $\mathbf{f}_\perp(s)$ is the Stokeslet strength's component which is perpendicular to the filament central axis. Therefore the sum of dipole and Stokeslets defines the flow induced by each segment of the helix body. As a result, there is a relation between the local velocity of a segment on the s location and the force per unit length;

$$\mathbf{u}(s) = -\frac{a^2 \mathbf{f}_\perp(s)}{4\mu} + \int_{|\mathbf{r}_0(s',s)| > \delta} \mathbf{f}(s') \cdot \mathbf{J}(\mathbf{r}_0) ds' \quad (2.73)$$

Where \mathbf{r}_0 is the vector from the point s on the central axis to the point s' and δ is a natural cutoff ($\delta = \frac{a\sqrt{e}}{2}$). For the spatial location r the Oseen tensor \mathbf{J} is;

$$J(\mathbf{r}) \equiv \frac{1}{8\pi\mu} \left(\frac{I}{|\mathbf{r}|} + \frac{\mathbf{r}\mathbf{r}^T}{|\mathbf{r}|^3} \right) \quad (2.74)$$

The thrust, torque and drag of the helical microswimmer can be obtained by applying rectangular rule of numerical integration and as a result we have;

$$J(\mathbf{r}) \equiv \frac{1}{8\pi\mu} \left(\frac{I}{|\mathbf{r}|} + \frac{\mathbf{r}\mathbf{r}^T}{|\mathbf{r}|^3} \right) \quad (2.75)$$

We need to parameterize spatial locations, so we define helical phase $\phi \equiv ks \cos(\theta)$ where $k = 2\pi/\lambda$ and $\mathbf{r} = R(\phi \cot(\theta), \cos(\phi), \sin(\phi))$. Therefore equation 2.73 is converted to following equation;

$$\mathbf{u}_n = \frac{(I - \hat{t}_n \hat{t}_n + D_n) \cdot \mathbf{f}_n}{4\pi\mu} + \frac{\mathbf{R} \Delta \phi \csc(\theta)}{8\pi\mu} \sum_{m \neq n} \frac{I + \hat{r}_{nm} \hat{r}_{nm}}{r_{nm}} \cdot \mathbf{f}_m + \Lambda(\Delta \phi) \quad (2.76)$$

Where $m, n = 1, 2, \dots, N$ and $\hat{t}_n = (\cos(\theta), -\sin(\theta) \sin(\phi_n), \sin(\theta) \cos(\phi_n))$. The position vector between spatial location is $\mathbf{r}_{nm} = \mathbf{r}(\phi_n) - \mathbf{r}(\phi_m)$.

The components of the velocity \mathbf{u}_n that are invariant alongside the helix can be obtained by integrating over the equation 2.76 and using the frame rotated with the helical phase. Then we can find the linear mapping between force and velocity per unit length and calculate rotational and translation velocity to find the force, torque and drag.

The first part of the equation 2.76 is called tensor D_n and it shows the helical segments that are centered at \mathbf{r} . D_n can be expressed in the form of following integral;

$$D_n = 1/2 \int_{|\mathbf{r}-\mathbf{r}_n| \in (\delta, \delta')} ds(\phi) \left(\frac{I}{|\mathbf{r} - \mathbf{r}_n|} + \frac{(\mathbf{r} - \mathbf{r}_n)(\mathbf{r} - \mathbf{r}_n)}{|\mathbf{r} - \mathbf{r}_n|^3} \right) \cdot \chi_z(\phi - \phi_n) \quad (2.77)$$

Where the rotation matrix χ_z is defined as;

$$\chi_z = \begin{bmatrix} \cos(\phi) & -\sin(\phi) & 0 \\ \sin(\phi) & \cos(\phi) & 0 \\ 0 & 0 & 1 \end{bmatrix} \quad (2.78)$$

We define new vectors for force and velocity to simplify the calculation;

$$\mathbf{u}_n' = \chi_z(-\phi_n) \cdot \mathbf{u} \quad (2.79)$$

$$\mathbf{f}_n' = \chi_z(-\phi_n) \cdot \mathbf{f} \quad (2.80)$$

Therefore the velocity \mathbf{u}_n' is invariant to the filament and the rotational and translational velocity of the helix can be written as;

$$\mathbf{u}_n' = (0, \mathbf{\Omega R}, U)^T \quad (2.81)$$

And the force;

$$\sum_{i=1} \mathbf{f}' \mathbf{R} \Delta \phi \csc \theta = (0, \mathbf{T}/\mathbf{R}, \mathbf{F}_x)^T \quad (2.82)$$

Therefore SBT can be expressed as;

$$\begin{aligned} \mathbf{u}_n' = & \frac{(I - \hat{t}_n \hat{t}_n + D_n) \cdot \mathbf{f}_n}{4\pi\mu} \\ & + \frac{\mathbf{R} \Delta \phi \csc(\theta)}{8\pi\mu} \sum_{m \neq n} \frac{\chi_z(\phi_m - \phi_n) + \chi_z(-\phi_n) \cdot \hat{r}_{nm} \hat{r}_{nm} \cdot \chi_z(-\phi_n)}{r_{nm}} \cdot \mathbf{f}_m' \\ & + \Lambda(\Delta \phi) \end{aligned} \quad (2.83)$$

Where both \hat{t}' and D_n' are invariant to the helical filament,

$$\hat{t}' = (0, \sin \theta, \cos \theta) \quad (2.84)$$

and

$$\hat{t}' = (0, \sin \theta, \cos \theta) \quad (2.85)$$

So we obtained the mapping between the force and velocity;

$$\begin{pmatrix} \mathbf{u}_1' \\ \mathbf{u}_2' \\ \vdots \\ \mathbf{u}_{N'}' \end{pmatrix} = \Delta \cdot \begin{pmatrix} \mathbf{f}_1' \\ \mathbf{f}_2' \\ \vdots \\ \mathbf{f}_{N'}' \end{pmatrix} \quad (2.86)$$

For the velocity $\mathbf{u}' = \mathbf{u}_n' = (0, \mathbf{\Omega R}, U)^T$ we have;

$$\begin{pmatrix} \mathbf{f}_1' \\ \mathbf{f}_2' \\ \vdots \\ \mathbf{f}_{N'}' \end{pmatrix} = \Delta^{-1} \cdot \begin{pmatrix} \mathbf{u}_1' \\ \mathbf{u}_2' \\ \vdots \\ \mathbf{u}_{N'}' \end{pmatrix} \quad (2.87)$$

Finally, the fluidic force and torque are;

$$(0, \frac{T}{R}, F_x)^T = \sum_{i=1}^N \mathbf{f}' \mathbf{R} \Delta \phi \csc \theta \quad (2.88)$$

2.3.2 Microrobot actuation

In this section the aim is to develop an algorithm for the microrobot velocity control. To achieve that, we need to figure out the direction that microrobot points out (\mathbf{X}_h) and then its rotational speed (Ω) to obtain a desired velocity [9]. In this algorithm, the only nonfluidic force is applied on the microrobot is its weight which expressed as $m\mathbf{g}$. The mass of the microrobot is m and the vector \mathbf{g} shows the acceleration gravity. The direction of the gravity is downward and represented by $\hat{\mathbf{g}} = \mathbf{g}/\|\mathbf{g}\|$.

Flowchart for Algorithm of the actuation method

Previous research on controlling a microswimmers's speed is evident that there is a lack of control if commanding microrobot with too rapid maneuvers [29] [28]. Therefore, in this work we assumed microswimmers can turn continuously to the aimed direction in such away that the temporary behavior is been ignored. We define $\tilde{\mathbf{X}}$ as the axis magnetic field should always be perpendicular to it. If the microrobot coordinate frame is aligned with the stationary world frame then there it does not require to convert vectors between these two frames. From the helical propulsion equation system, we specifically considering the first equation which is the relation between non-fluidic force, angular and translational velocity of the microswimmer.

$${}^h\mathbf{f} = {}^h\mathbf{A}{}^h\mathbf{V} + {}^h\mathbf{B}{}^h\boldsymbol{\omega} \quad (2.89)$$

The matrix ${}^h\mathbf{A}$ is invertible, thus the desired velocity can be obtained from the equation 2.89;

$${}^h\mathbf{V} = ({}^h\mathbf{A}^{-1}){}^h\mathbf{f} + (-{}^h\mathbf{A}^{-1}{}^h\mathbf{B}){}^h\boldsymbol{\omega} = {}^h\mathbf{D}{}^h\mathbf{f} + {}^h\mathbf{E}{}^h\boldsymbol{\omega} \quad (2.90)$$

$${}^h\mathbf{D}_h = \begin{bmatrix} d_{11} & 0 & 0 \\ 0 & d_{22} & 0 \\ 0 & 0 & d_{22} \end{bmatrix} \quad (2.91)$$

$${}^h\mathbf{E}_h = \begin{bmatrix} e_{11} & 0 & 0 \\ 0 & e_{22} & 0 \\ 0 & 0 & e_{22} \end{bmatrix} \quad (2.92)$$

The equations 2.90, 2.91, 2.92 are in the helix frame and can be converted to the world frame by applying relation matrix ${}^w\mathbf{R}_h$ on the equation 2.90;

$${}^w\mathbf{R}_h{}^h\mathbf{V} = {}^w\mathbf{R}_h{}^h\mathbf{D}{}^h\mathbf{f} + {}^w\mathbf{R}_h{}^h\mathbf{E}{}^h\boldsymbol{\omega} \quad (2.93)$$

$${}^w\mathbf{V} = {}^w\mathbf{E}{}^w\boldsymbol{\omega} + {}^w\mathbf{D}{}^w\mathbf{f} \quad (2.94)$$

Then by applying the similar transformation to other component 2.91, 2.92;

$${}^w\mathbf{V} = {}^w\mathbf{R}_h {}^h\mathbf{V} \quad {}^w\mathbf{f} = {}^w\mathbf{R}_h {}^h\mathbf{f} \quad {}^w\mathbf{D} = {}^w\mathbf{R}_h {}^h\mathbf{D} {}^h\mathbf{R}_w \quad {}^w\mathbf{E} = {}^w\mathbf{R}_h {}^h\mathbf{E} {}^h\mathbf{R}_w \quad (2.95)$$

To obtain ${}^h\mathbf{R}_w$ the orientation of the microrobot is required to be detected whilst it is rotating during propulsion around the axis which is difficult. For that reason, the equation 2.94 is expressed in such way that it does not require to know the microrobot orientation whilst rotating about its central axis. Since the microrobot is torque driven and the only nonfluidic force is involved in equation 2.89 is its weight ($m\mathbf{g}$). The velocity of microrobot can be decomposed to vertical and horizontal components:

$$\mathbf{V}_{ver} = (\mathbf{V} \cdot \hat{\mathbf{g}}) \hat{\mathbf{g}} \quad (2.96)$$

$$\mathbf{V}_{hor} = \mathbf{V} - \mathbf{V}_{ver} \quad (2.97)$$

Two options can be considered for the $\|\mathbf{V}_{hor}\|$:

$$\|\mathbf{V}_{hor}\| = 0 \quad , \quad \|\mathbf{V}_{hor}\| \neq 0 \quad (2.98)$$

The first option is a trival case, because when the microrobot is being commanded with $\|\mathbf{V}_{hor}\| = 0$, that means the microrobot only swim vertically in either directions according to the equation 2.97. This is the spacial case when the six degree of freedom microrobot will effectively become the microrobot with two degree of freedom which is pointing in the direction of the gravity acceleration and its angular velocity can be found directly from the equation 2.94:

$$\boldsymbol{\Omega} = \frac{\|\mathbf{V}\| + d_{11}\|\mathbf{f}\|}{e_{11}} \quad , \quad \tilde{\mathbf{X}} = -\hat{\mathbf{g}} \quad (2.99)$$

The second option $\|\mathbf{V}_{hor}\| \neq 0$ is more challenging, because it is required to set the coordinate frame for microrobot which does not rotate when the it is rotating around the central axis. The ideal coordinate frame can be constructed by using $\hat{\mathbf{g}}$ and based on the eigenvectors ⁵ of ${}^w\mathbf{D}$ or ${}^w\mathbf{E}$. This coordinate system is denoted by p and can be defined as :

$$\mathbf{x}_p = \frac{(\mathbf{x}_h \cdot \mathbf{V}) \mathbf{x}_h}{|\mathbf{x}_h \cdot \mathbf{V}|} \quad (2.100)$$

$$\mathbf{y}_p = \frac{(\mathbf{x}_p \times \mathbf{g})}{\|\mathbf{x}_p \times \mathbf{g}\|} \quad (2.101)$$

$$\mathbf{z}_p = \mathbf{x}_p \times \mathbf{y}_p \quad (2.102)$$

⁵If we have a set of data point, the set can be deconstructed into eigenvector and eigenvalue where eigenvector is the direction that data spread out and eigenvalue is the variance of the data in that direction. The principle component is the eigen vector with the largest eigenvalue [2].

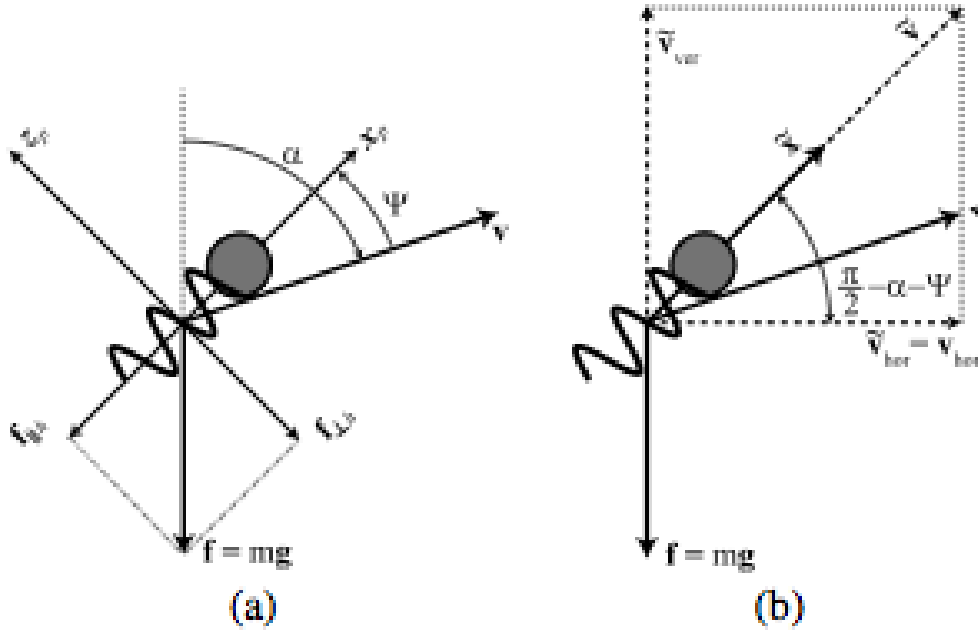


Figure 2.10: (a) The principle coordinate frame based on the gravity and principle components of the matrices in equations 2.92 and 2.91. (b) Construction details of direction of the microswimmer ($\tilde{\mathbf{X}}$) [9].

The new (principle) coordinate system will solve the problem because it is invariant to the rotation of the microswimmer around its central axis. Therefore the equation 2.94 can be expressed in terms of the principle coordinate frame. In the following paragraph We first configure the representation for the first component (${}^w\mathbf{E}^w\boldsymbol{\omega}$) of the equation 2.94 and followed by similar process on the second component (${}^w\mathbf{D}^w\mathbf{f}$). The final result will express the desired velocity vector in terms of the principal coordinate system.

It is assumed that the microrobot is at steady state, that means ${}^w\boldsymbol{\omega} = \Omega\tilde{\mathbf{x}} = \Omega^w\mathbf{x}_p$, also we know two vectors ${}^w\mathbf{x}_p$ and ${}^w\mathbf{x}_h$ are parallel. It has been proved that ${}^h\mathbf{x}_h$ and e_{11} are eigenvector and eigenvalue of matrix ${}^h\mathbf{E}$ respectively [9]. The transformation matrix ${}^w\mathbf{R}_h$ will not affect the eigenvalue (e_{11}) but it will rotate the eigenvector (${}^h\mathbf{x}_h$) from the helix coordinate frame to the global frame (w). As a result (e_{11}) and (${}^w\mathbf{x}_p$) are the eigenvalue and eigenvector in the world coordinate system respectively. By considering the vectors ${}^w\mathbf{x}_p$ and ${}^h\mathbf{x}_p$ are parallel and definition of eigenvalue and eigenvector ⁶ the first component of the desired velocity (${}^w\mathbf{E}^w\boldsymbol{\omega}$) can be represented in the principle coordinate system as follow:

$${}^w\mathbf{E}^w\boldsymbol{\omega} = {}^w\mathbf{E}\Omega^w\mathbf{x}_p = e_{11}\Omega^w\mathbf{x}_p \quad (2.103)$$

The similar reasoning has been used to represent the second component (${}^w\mathbf{D}^w\mathbf{f}$) of the velocity equation (2.94) in terms of the principle coordinate system. In this case, d_{11} and d_{22} are eigenvalues of the matrix ${}^h\mathbf{D}$ such that ${}^h\mathbf{x}_h$ is the eigenvector corresponding to

⁶Assume A is a square matrix $n \times n$, we call λ an eigenvalue of matrix A if the non-zero vector \mathbf{V} exists such that $A\mathbf{V} = \lambda\mathbf{V}$. The vector \mathbf{V} is called eigenvector corresponding to eigenvalue λ . [1].

the d_{11} and d_{22} is associated with an eigenspace⁷ spanned by $\{{}^h\mathbf{y}_h, {}^h\mathbf{z}_h\}$. Again, the eigenvalues and eigenspace will remain unaffected under transformation matrix. Thus, the eigenvalue d_{11} is corresponding to the ${}^w\mathbf{x}_h$ and the eigenvalue d_{22} is related to the vector in the subspace $\{{}^w\mathbf{y}_h, {}^w\mathbf{z}_h\}$. In addition the force vector can be decomposed into two vectors; one parallel to the central axis of helix and the other perpendicular to that axis (${}^w\mathbf{x}_h$):

$${}^w\mathbf{f} = ((\mathbf{f}.\mathbf{x}_h){}^w\mathbf{x}_h) + ((\mathbf{f}.\mathbf{y}_h){}^w\mathbf{y}_h + (\mathbf{f}.\mathbf{z}_h){}^w\mathbf{z}_h) = {}^w\mathbf{f}_{\parallel h} + {}^w\mathbf{f}_{\perp h} \quad (2.104)$$

If ${}^w\mathbf{f}_{\perp h}$ does not change then both ${}^w\mathbf{f}$ and ${}^w\mathbf{f}_{\parallel h}$ will not change if microrobot rotate around its central axis. In addition, ${}^w\mathbf{y}_p$ and ${}^w\mathbf{z}_p$ are in the eigenspace formed by $\{{}^w\mathbf{y}_h, {}^w\mathbf{z}_h\}$. As a result, ${}^w\mathbf{f}_{\perp h}$ can be written in the principle coordinate frame as a linear combinations of two vectors ${}^w\mathbf{z}_p$ and ${}^w\mathbf{y}_p$. Because d_{22} is the corresponding eigenvalue of any vector in the span of the $\{{}^w\mathbf{y}_h, {}^w\mathbf{z}_h\}$, so it will be the eigenvalue associated with ${}^w\mathbf{f}_{\perp h}$. Using the fact that d_{11} is the eigenvalue corresponding to ${}^w\mathbf{f}_{\parallel h}$ and implying the transformation matrix we can write the force based on the principle component axis:

$$\begin{aligned} {}^w\mathbf{D}{}^w\mathbf{f} &= {}^w\mathbf{D}{}^w\mathbf{f}_{\parallel h} + {}^w\mathbf{D}{}^w\mathbf{f}_{\perp h} = d_{11}{}^w\mathbf{f}_{\parallel h} + d_{22}{}^w\mathbf{f}_{\perp h} \\ &= d_{11}(\mathbf{f}.\mathbf{x}_p){}^w\mathbf{x}_p + d_{22}(\mathbf{f}.\mathbf{z}_p){}^w\mathbf{z}_p \end{aligned} \quad (2.105)$$

Both components of the desired velocity are written on the basis of the principle components. By replacing equations 2.103 and 2.105 in equation 2.94 we have:

$${}^w\mathbf{V} = d_{11}(\mathbf{f}.\mathbf{x}_p){}^w\mathbf{x}_p + d_{22}(\mathbf{f}.\mathbf{z}_p){}^w\mathbf{z}_p + e_{11}\Omega{}^w\mathbf{x}_p \quad (2.106)$$

Therefore, none of the component of the velocity will be change when microrobot rotates around the central axis.

Since $\|\mathbf{V}_{hor}\| \neq 0$, as it is shown in the Fig 2.10 we can define the angle α between the vector \mathbf{v} and the vertical axis in the world frame.

$$\alpha = \tan^{-1}(\|\mathbf{V}_{hor}\|/\|\mathbf{V}_{ver}\|) \quad (2.107)$$

The microrobot requires to be position above the desired velocity vector (upward) with the angle ψ to compensate for the gravity vector. If we project the the desired velocity equation (2.106) into principle coordinate axis then we have:

$$(\mathbf{V}.\mathbf{x}_p) = d_{11}(\mathbf{f}.\mathbf{x}_p) + e_{11}\Omega \quad (2.108)$$

$$(\mathbf{V}.\mathbf{z}_p) = d_{22}(\mathbf{f}.\mathbf{z}_p) \quad (2.109)$$

⁷Let A be a $n \times n$ square matrix with an eigenvalue λ . Then the union of all eigenvectors associated with the eigenvalue λ and vector zero is a subspace of \mathbb{R}^3 which is called the eigenspace for the eigenvalue λ . [25].

As it can be seen in the Fig 2.10, the both side of the equation 2.109 can be replaced by its equivalents:

$$(\mathbf{V}.\mathbf{z}_p) = -\|\mathbf{V}\| \sin(\psi) \quad (2.110)$$

$$(\mathbf{f}.\mathbf{z}_p) = \|\mathbf{f}\| \sin(\psi - \alpha) \quad (2.111)$$

Thus, the replacing will lead to the following:

$$-\|\mathbf{V}\| \sin(\psi) = d_{22}\|\mathbf{f}\| \sin(\psi - \alpha) \quad (2.112)$$

by applying the subtraction law for $\sin(\psi - \alpha)$ ⁸, the angle ψ can be obtained from the following equation:

$$\psi = \tan^{-1} \frac{(d_{22}\|\mathbf{f}\| \sin(\alpha))}{\|\mathbf{V}\| + d_{22}\|\mathbf{f}\| \cos(\alpha)} \quad (2.113)$$

All the parameters in the above equation are known and the direction point ($\tilde{\mathbf{X}}$) of the microrobot can be reconstructed by using angles α and ψ and defining a dummy vector $\tilde{\mathbf{V}}$ such that $\tilde{\mathbf{V}} = \tilde{\mathbf{V}}_{ver} + \tilde{\mathbf{V}}_{hor}$ where $\tilde{\mathbf{V}}_{ver} = -\|\tilde{\mathbf{V}}_{hor}\| \tan(\pi/2 - \alpha + \psi)\hat{\mathbf{g}}$ and $\tilde{\mathbf{V}}_{hor} = \mathbf{V}_{hor}$. Therefore the final solution for the direction point is:

$$\tilde{\mathbf{X}} = \frac{\tilde{\mathbf{V}}}{\|\tilde{\mathbf{V}}\|} \quad (2.114)$$

Therefore the angular velocity (Ω) will be derived from equation 2.108, considering that $(\mathbf{V}.\mathbf{x}_p) = \|\mathbf{V}\| \cos(\psi)$ and $(\mathbf{f}.\mathbf{x}_p) = -\|\mathbf{f}\| \cos(\psi - \alpha)$:

$$\Omega = \frac{\|\tilde{\mathbf{V}}\| \cos(\psi) + d_{11}\|\mathbf{f}\| \cos(\psi - \alpha)}{e_{11}} \quad (2.115)$$

At this point the rotational velocity of microrobot can be used to compute the magnetic torque according to the following equasion from propulsion equasion system;

$$\tau = \mathbf{B}\mathbf{V} + \mathbf{C}\Omega \quad (2.116)$$

Where \mathbf{V} is known and \mathbf{B} and \mathbf{C} are precomputed from coefficient matix. Then considering magnetic torque equasion and replacing torque by its equivalent 2.116;

$$\tau = \mathbf{V}M \times \mathbf{B} \quad (2.117)$$

Where M magnetisation constant and V is a volume of the magnetic object. Finally, the electric current (i) is required to generate a dynamic magnetic field is achieved by the following;

⁸ $\sin(\psi - \alpha) = \sin(\psi) \cos(\alpha) - \cos(\psi) \sin(\alpha)$

$$|\mathbf{B}| = \left(\frac{b^2}{(b^2 + l^2)^{3/2}}\right)\mu_0 i \quad (2.118)$$

And the simulation algorithm is completed.

Chapter 3: Results

In this chapter all the result will be presented under two sections. In the following section the result of implementing three propulsion methods is demonstrated.

3.1 Design and propulsion methods

3.2 Design and fabrication

The design of microrobot has been done by the software design c

Chapter 4: Discussion

Compare force driven and torque driven algorithms.

Rodenborn et al. [20] demonstrated the failure of resistive force theory to predict thrust and drag in microrobots motion accurately. The reason of the failure was neglecting hydrodynamic interaction between flows induced by different parts of a flagellum. In particular, helical flagellum with smaller pitch (λ) will have smaller separation of filament segments (Figure 2.5). Hence, the hydrodynamic interaction between different parts of a flagellum becomes stronger and in very small pitch ($\lambda \rightarrow 0$) the helix converts to a cylinder which has no thrust ($F = 0$).

Chapter 5: Conclusion and future work

References

- [1] Harvey Mudd College. Eigenvectors and eigenvalues @ONLINE, November 2013. URL <https://www.math.hmc.edu/calculus/tutorials/eigenstuff/eigenstuff.pdf>.
- [2] George Dallas. Principal component analysis 4 dummies: Eigenvectors, eigenvalues and dimension reduction @ONLINE, October 2013. URL <http://georgemdallas.wordpress.com/2013/10/30/principal-component-analysis-4-dummies-eigenvectors-eigenvalues-and-dimension-reduction/>.
- [3] Jon Edd, Sébastien Payen, Boris Rubinsky, Marshall L Stoller, and Metin Sitti. Biomimetic propulsion for a swimming surgical micro-robot. In *Intelligent Robots and Systems, 2003.(IROS 2003). Proceedings. 2003 IEEE/RSJ International Conference on*, volume 3, pages 2583–2588. IEEE, 2003.
- [4] Wei Gao, Xiaomiao Feng, Allen Pei, Christopher R Kane, Ryan Tam, Camille Hennessy, and Joseph Wang. Bioinspired helical microswimmers based on vascular plants. *Nano letters*, 14(1):305–310, 2013.
- [5] Sangwon Kim, Famin Qiu, Samhwan Kim, Ali Ghanbari, Cheil Moon, Li Zhang, Bradley J Nelson, and Hongsoo Choi. Fabrication and characterization of magnetic microrobots for three-dimensional cell culture and targeted transportation. *Advanced Materials*, 25(41):5863–5868, 2013.
- [6] Youngho Ko, Sungyoung Na, Youngwoo Lee, Kyoungrae Cha, Seong Young Ko, Jongoh Park, and Sukho Park. A jellyfish-like swimming mini-robot actuated by an electromagnetic actuation system. *Smart Materials and Structures*, 21(5):057001, 2012.
- [7] Eric Lauga, Willow R DiLuzio, George M Whitesides, and Howard A Stone. Swimming in circles: motion of bacteria near solid boundaries. *Biophysical journal*, 90(2):400–412, 2006.
- [8] MJ Lighthill. Large-amplitude elongated-body theory of fish locomotion. *Proceedings of the Royal Society of London. Series B. Biological Sciences*, 179(1055):125–138, 1971.
- [9] Arthur W Mahoney, John C Sarrazin, Eberhard Bamberg, and Jake J Abbott. Velocity control with gravity compensation for magnetic helical microswimmers. *Advanced Robotics*, 25(8):1007–1028, 2011.
- [10] Roger McFadden. A basic introduction to clean rooms @ONLINE, 2014. URL <http://www.coastwidelabs.com/>.

- [11] A J Mestel. Biofluids lecture 3: Flagellar swimming, resistive force theory @ONLINE, January 2013. URL <http://www2.imperial.ac.uk/~ajm8/BioFluids/>.
- [12] nanoscribe. nanoscribe @ONLINE, February 2014. URL <http://www.nanoscribe.de/en/>.
- [13] Kathrin E Peyer, Erdem C Siringil, Li Zhang, Marcel Suter, and Bradley J Nelson. Bacteria-inspired magnetic polymer composite microrobots. In *Biomimetic and Biohybrid Systems*, pages 216–227. Springer, 2013.
- [14] Kathrin E Peyer, Soichiro Tottori, Famin Qiu, Li Zhang, and Bradley J Nelson. Magnetic helical micromachines. *Chemistry-A European Journal*, 19(1):28–38, 2013.
- [15] Kathrin E Peyer, Li Zhang, and Bradley J Nelson. Bio-inspired magnetic swimming microrobots for biomedical applications. *Nanoscale*, 5(4):1259–1272, 2013.
- [16] Edward M Purcell. The efficiency of propulsion by a rotating flagellum. *Proceedings of the National Academy of Sciences*, 94(21):11307–11311, 1997.
- [17] Famin Qiu, Rami Mhanna, Li Zhang, Yun Ding, Satoshi Fujita, and Bradley J Nelson. Artificial bacterial flagella functionalized with temperature-sensitive liposomes for controlled release. *Sensors and Actuators B: Chemical*, 2014.
- [18] Famin Qiu, Li Zhang, Kathrin E Peyer, Marco Casarosa, Alfredo Franco-Obregón, Hongsoo Choi, and Bradley J Nelson. Noncytotoxic artificial bacterial flagella fabricated from biocompatible ormocomp and iron coating. *Journal of Materials Chemistry B*, 2(4):357–362, 2014.
- [19] Tian Qiu, John G Gibbs, Debora Schamel, Andrew G Mark, Udit Choudhury, and Peer Fischer. From nanohelices to magnetically actuated microdrills: a universal platform for some of the smallest untethered microrobotic systems for low reynolds number and bio-logical environments.
- [20] Bruce Rodenborn, Chih-Hung Chen, Harry L Swinney, Bin Liu, and HP Zhang. Propulsion of microorganisms by a helical flagellum. *Proceedings of the National Academy of Sciences*, 110(5):E338–E347, 2013.
- [21] David J Smith. A boundary element regularized stokeslet method applied to cilia-and flagella-driven flow. *Proceedings of the Royal Society A: Mathematical, Physical and Engineering Science*, 465(2112):3605–3626, 2009.
- [22] Soichiro Tottori and Bradley J Nelson. Artificial helical microswimmers with mastigoneme-inspired appendages. *Biomicrofluidics*, 7(6):061101, 2013.
- [23] Soichiro Tottori, Li Zhang, Famin Qiu, Krzysztof K Krawczyk, Alfredo Franco-Obregón, and Bradley J Nelson. Magnetic helical micromachines: fabrication, controlled swimming, and cargo transport. *Advanced materials*, 24(6):811–816, 2012.
- [24] Purdue University. Scanning electron microscope @ONLINE, January 2014. URL <http://www.purdue.edu/ehps/rem/rs/sem.htm>.
- [25] Eric Weisstein. Eigenspace @ONLINE, August 2014. URL <http://mathworld.wolfram.com/Eigenspace.html>.
- [26] Frank M White and Isla Corfield. *Viscous fluid flow*, volume 3. McGraw-Hill New York, 1991.

-
- [27] Wang Xi, Alexander A. Solovev, Adithya N. Ananth, David H. Gracias, Samuel Sanchez, and Oliver G. Schmidt. Rolled-up magnetic microdrillers: towards remotely controlled minimally invasive surgery. *Nanoscale*, 5:1294–1297, 2013.
 - [28] Li Zhang, Jake J Abbott, Lixin Dong, Bradley E Kratochvil, Dominik Bell, and Bradley J Nelson. Artificial bacterial flagella: Fabrication and magnetic control. *Applied Physics Letters*, 94(6):064107, 2009.
 - [29] Li Zhang, Jake J Abbott, Lixin Dong, Kathrin E Peyer, Bradley E Kratochvil, Haixin Zhang, Christos Bergeles, and Bradley J Nelson. Characterizing the swimming properties of artificial bacterial flagella. *Nano Letters*, 9(10):3663–3667, 2009.